

The tempest in a cubic millimeter: Image-based refinements necessitate the reconstruction of 3D microvasculature from a large series of damaged alternately-stained histological sections

Oleg Lobachev

Hannover Medical School, OE 4120, Carl-Neuberg-Straße 1, 30625 Hannover, Germany

This work presents two methods that facilitate a 3D reconstruction of microscopic blood vessels in the volume slightly larger than 1 mm^3 . The source of the data are histological serial sections, i.e., microscopic images of probes, stained with immunohistochemistry. Odd and even sections have different stainings in our primary data set. Thus, firstly, an approach to register an alternately-stained series is presented. With image filtering and a feature-detection-based registration we obtain a registered stack of 148 serial sections. The series has missing sections, locally damaged sections, artifacts from acquisition. All these hinder correct connectivity of blood vessels. With our second approach we interpolate the missing information while maintaining the connectivity. We achieve this with deformations based on dense optical flow. The presented methodology is applicable to further histological series. A combination of both approaches allows us to reconstruct more than 76% larger volumes. An important detail was the composition mode of images. Summarizing, we use methods from image processing and computer vision to create large-scale 3D models from immunostained histological serial sections.

I. INTRODUCTION

Histological serial sections are the method of choice for obtaining insights from human tissues at microscopic levels. Despite the availability of further imaging techniques, ranging from micro-CT to two-photon microscopy, there is de-facto no choice when working with human specimens. Micro-CT lacks on resolution and does not allow for labeling of specific cells. Nano-CT has too small working area. Virtually all recently developed imaging methods focus on model organisms. In them, artificial enhancements are possible, including fluorescent proteins, artificially-transparent tissues (incl. “clarity”), and further modifications that facilitate novel imaging methods. Those cannot be thought of with humans; the specimens need to be processed as they are. Immunohistology introduced a much more precise staining. With immunohistology, specific molecules can be visualized by “connecting” them to the antibodies that in their turn make the color pigment solution precipitate where the sought-for molecules were in the first place. Those molecules are not necessarily unique, but in most cases, morphological differences between different cell types exhibiting the same molecule is large enough for a proper diagnosis. For an introduction to histology, consult, e.g., ref. [58].

A single histological section, even with immunostaining, does not suffice for a proper understanding. The sections are very thin (typically about $7\text{ }\mu\text{m}$ in standard sections, starting from $1\text{ }\mu\text{m}$ in semi-thin sections), but cover a larger area (about 1 cm^2). This yields a de-facto two-dimensional representation of the tissue. In longer-spawning entities, such as blood vessels or nerves, very little insight can be derived from a single section. Fortunately, a series of histological sections, the so-called serial sections, can be sectioned, stained, and processed.

The best way of facilitating better understanding from serial sections is to perform a full-fledged 3D reconstruction

[66]. The path to it is, however, long and problematic. A proper registration of the serial sections needs to be established [68]. The sections can vary in thickness and hence in intensity. They need to be normalized [53]. In further processing, a correct separation of colors in the staining [78], faithful selection of the shape, correct mesh construction [69] and mesh processing should follow. The presentation of the final reconstruction to the experts is also an issue. The interaction of the experts with the model, the so-called visual analytics, is the actual way of finding insights and producing results. We developed a virtual reality application for this sake [66, 99, 101].

This paper, however, focuses on the cases when not everything works well in the required biomedical processing and the above 3D reconstruction pipeline. The reasons vary greatly, but in many cases the result is the same: A section or a part thereof is not available for the 3D reconstruction.

Previously, the only definite way of coping with such problems was to truncate the series. While this is the most pure and not disputable approach, the amount of data to be discarded is quite extreme. In the series we mostly focus on this paper, 150 sections were produced, first and last were controls and were not indented for the 3D reconstruction. Due to problems during biological processing, 25 sections in the beginning of the series could not be fully used. Two sections were outright lost. Acquisition of such a large data set is a tedious and error-prone process. Because of some focusing problems, not all section images were usable. When the series was truncated to mitigate all above problems, only 83 to 91 sections were usable in varying regions. This constitutes up to 44.67% of lost sections. (Fig. 1 presents a truncated and a healed mesh.) With the methods presented here, we were able to salvage the damaged regions and to bridge over the lost sections, reconstructing all 148 immunostained sections. We operate on a region of interest (ROI) of $2k \times 2k$ pixels,

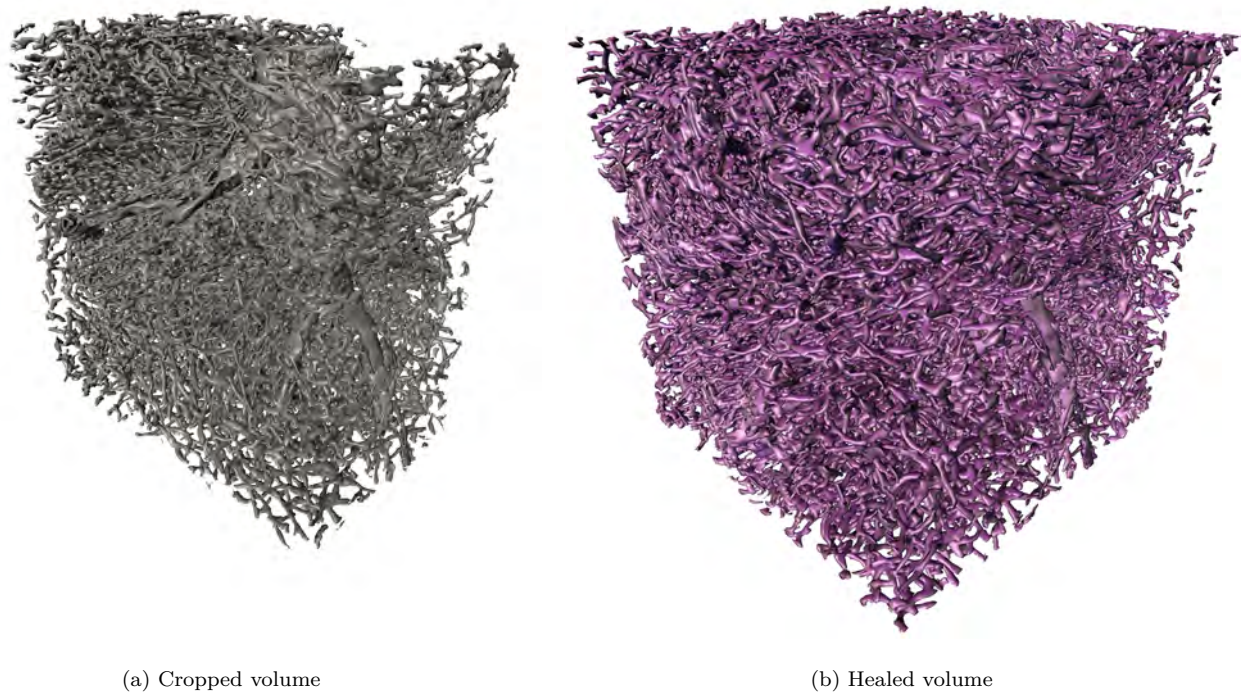


Figure 1: Motivation for this paper: healing greatly increases the amount of information available for analysis. Here, two decimated meshes are presented, which were reconstructed at same iso-value 120 from corresponding volumes. The meshes are rendered from the same view point. Fig. (a) shows a reconstruction from 84 sections available in the current region without healing. In (b) the result of our healing method is presented, all 148 immunostained sections are used. Notice also the high degree of complexity and self-occlusion. Fig. 9 compares the full meshes. The x and y sides of the reconstructions (the wider sides in (a)) span over 1 mm.

yielding a 3D reconstruction of more than 1 mm^3 of human splenic tissue at acquisition resolution of $0.5\text{ }\mu\text{m}/\text{pixel}$.

A. Related Work

There is a lot of related work on registration, including co-registration of different stainings (Section I A 1) and co-registration of other modalities (Section I A 2). There is virtually no related work on the repair of histological sections (Section I A 3). We also present an overview of related deep learning approaches (Section I A 4) and mention the methods we use for evaluation in Section I A 5.

1. Registration of serial sections

Ourselin et al. [80] presented one of the first fully automatic approaches for the “normal” registration of serial sections. Pichat et al. [84] feature a recent review.

In this work we utilize our feature-based non-rigid method [68, 106] for the actual registration of the whole series, extending it to work with alternating staining. In has been also previously used for a fine-grain registration. For a pairwise deformation of neighboring sections, we

also used *elastix* [55].

Kajihara et al. present a framework for registration of serial sections [51]. They perform a RANSAC-based rigid registration based on feature detection first, and then an as-rigid-as-possible region-based registration from key-point correspondences is used. The regions emerge from clustering keypoints. Then, local transforms are blended together to obtain a non-rigid transformation. (In a contrast, our registration method [68] uses keypoint detection and matching; then RANSAC for the rigid phase; then non-rigid alignment is hierarchically computed from the neighborhood matches for the whole series of sections, producing a global pyramid of non-rigid transformations.) Since Kajihara et al. are concerned with larger series, a sudden discontinuity in registration is mitigated by manual selection of a reference. Our work is focused on an automatic registration (with possible manual removal of an offending image yielding a discontinuity) and, mostly important, the repair of the damage caused by such a removal or by inevitable processing and acquisition artifacts.

The remaining part of this section handles co-registration, i.e., the registration of differently stained sections. Refs. [19, 56] rely on the segmentation of „common ground“ between the different stainings. Similarly

do Wentzensen et al. [110] and Braumann et al. [18], as Wentzensen et al. register three different stainings to each other by the means of a segmentation. They applied some sophisticated sampling strategies and used a fuzzy classification of the segmented stainings. We recovered our similarity information in a pretty different manner.

With a similar goals Mueller et al. [77] focus on deformable registration of whole routine sections for digital pathology, involving elastix [55] and mutual information with additional constraints. Our work focuses on immunohistological stainings.

Mosaliganti et al. [76] developed a registration method for larger stacks and were bound to introduce “a mixture of automated and semi-automated enhancements”. Our registration method is fully automated. User input was only used to determine the masks during “partial image” healing sessions.

Lippolis et al. [63] perform co-registration of biopsies or removed organs, combining H&E, immunohistochemistry, and a fluorescence marker. They use RANSAC-based rigid registration, we co-register two immunohistological stainings and perform also multiple non-rigid steps. du Bois d’Aische et al. [31] register micro to macro images in a complex framework. We focus on one magnification level.

Jiang et al. [48] hierarchically co-registered H&E and immunohistochemistry (Caspase3, KI67 and PHH3) with image-patch-based method, involving FFT followed by kernel density estimation. They obtained the ground truth for the evaluation from manual registration. We used a fully different method stack for the registration, our evaluation is based on similarity metrics and 3D reconstruction; however our images feature a different grade of similarity.

Song et al. [96] use unsupervised classification for a co-registration of differently-stained serial sections. We pursue a fully different approach as our alternating series have some “common ground”. Ref. [105] develops a tool for a more comfortable diagnosis with co-registered differently-stained sections. They use chamfer matching for the registration. This work focuses on alternating series and repair of missing sections. Our series is co-registered to form a common volume, our evaluation [100] focuses on the analysis of the 3D models in virtual reality. Section IV 1 a discusses the methodological difference between the related work and our method.

2. Co-registration in other modalities

Ashburner and Friston [6] co-register neuroimages using affine transformation and clustering on segmented images. Another early attempt was performed by Andersson et al. [5].

Bardinet et al. [12] have co-registered some serial sections and MRI of human brain. The utilized sections were, however, visually quite similar to MRI cross-sections (and additionally processed to increase the similarity). A

registration of serial sections to the block face images (photographs of the probe before this particular section was made) has been used [82, 92] as a proxy for the registration with coarser, but inherently 3D data, such as MRI.

Michálek et al. [74] co-registered matrix-assisted laser desorption/ionization mass spectrometry and confocal fluorescence microscopic images. Such images have drastically different resolutions. Lorenzen et al. [70] co-registered different MR modalities (i.e., data from inherently 3D acquisitions) of the same brain. Ourselin et al. [81] parallelized the co-registration of MRI and CT data with the goal of a clinical use.

Lee et al. [59] are concerned with learning a similarity measure from aligned 3D images and then apply it to a rigid multimodal registration. Tang et al. [102] have a similar idea, but perform a deformable registration on MRI and CT. Heinrich et al. [42] derive a modality-independent descriptor and use it in multimodal MRI and CT registration.

Wachinger and Navab [107] derive a similarly looking representation from various modalities of 3D images and use it for registration. Haber and Modersitzki [41] introduce a different image similarity metric for multimodal registration of inherently 3D medical images. Gehring et al. [36] co-register optoacoustic tomography data with MRI. Becker et al. [13] co-register micro-CT with histological sections with chamfer matching. Such co-registrations have clinical impact, e.g., [8, 60, 90]. A separate topic is a groupwise image registration, typically performed on MRI data, [11, 14, 15, 44, 45, 86, 111].

The actual idea of a co-registration is much broader, it has been used, e.g., in synthetic aperture radars [61] or mass spectrometry [83].

3. Repair of damaged series

The quite wide-spread problem of damaged sections is not often mentioned in the literature, as it is widely regarded to be a technical issue.

Song et al. [97] are aware of the missing sections problem, no repair is performed, but attempts to recover the missing information in order to maintain the registration; naturally, their method loses precision in such cases. Burton et al. [21] mention the missing sections problem; missing data is approximated by averaging nearest neighbor sections. In this work we perform a more elaborate repair, involving optical flow and a meaningful blending.

In case of a missing section, Saleem and Logothetis [91] sketch drawings from previously obtained MRI. In a contrast, we derive information from neighboring sections.

Alic et al. [2] are aware of possibly damaged sections, but do not elaborate. They co-register MR and histological images with larger (60 μm) distance between sections, using a manual and derived-from-manual segmentations. Their registration of serial sections uses mutual information. We use automatic key-point-based matching.

Generation of intermediate sections for 3D reconstruction from microscopic data has been suggested before [22, 67], however the method presented here differs in goal, details of blending, and in using registration prior to the computation of optical flow. A comparison with existing methods is in Section IV 1 b.

4. Deep learning

Lai [57], Litjens et al. [64, 65], Zhou et al. [116], Ker et al. [52] and Altaf et al. [4] provide an overview of modern machine learning techniques in application to medical imaging. Garcia-Garcia et al. [35] provide a review of machine learning techniques w.r.t. general segmentation.

Further papers [23, 30, 34, 71, 75, 87, 104, 108, 112, 113] highlight specific applications of machine learning to medical segmentation or further (medical) image processing. Ref. [24] is a current result in semantic segmentation. Quite a few [25, 72, 73, 94] have utilized deep learning to perform a multimodal registration. Deep learning is also used for the separation of staining colors [3, 3, 20, 39, 93] or for registration [10, 27, 28].

We do not use any neural networks in this work, but utilize conservative image processing and computer vision repertoire.

5. Evaluation

We use dense optical flow [32] (see [9] for a review), Jaccard measure [46], and SSIM [109] to visually quantify the quality of our healing (Section III 1). The actual assessment can only happen through the evaluation of the quality of resulting 3D reconstructions (Section III 3). We use geodesic distance computations on the mesh [26, 29] for such an evaluation. (A recent development in this area is, e.g., ref. [79].)

B. Contributions

Firstly, we present a method to “lift” a registration method to alternating stainings of histological serial sections, in case there is a common ground between stainings. Secondly, we introduce a novel method to repair damaged or missing sections in the series. Our method is able to maintain the microvessel connectivity. Thus, the size of section series available for a 3D reconstruction is largely enhanced. In our running example, the amount of sections increased from 84 to 148, i.e., an increase of more than 76 %. With the presented method we were able to reconstruct the vasculature in slightly over 1 mm³ of tissue at a microscopic resolution.

II. METHODS

A. Data

1. Data origin and description of the data set

We were primarily working with 148 serial sections from the spleen of a 22-year-old male, acquired in 2000. The ethics of work with human materials fulfilled local regulations of the Philipps-University Marburg at the time of acquisition. The goal of the study was to investigate the capillary sheaths and the distribution of B-lymphocytes. The sections were *alternatively* stained for CD34 (cells in the walls of blood vessels, blue), SMA (some supporting structures and environments of arterioles, larger blood vessels, brown), and either CD271 (capillary sheaths and weakly some cells in the follicles, red) or CD20 (B-lymphocytes, red). Fig. 2 provides an overview.

The sections were processed for the transmitted light microscopy. This decision was made because of the established staining procedures and because the transmitted light stainings are permanent and can be stored and re-examined over decades.

The sections were digitized using Leica SCN 400 scanning microscope with a 20× lens. The final resolution was 0.5 μm/ pixel, full sections spanning approx. 8 mm × 11 mm were captured. A single section was 7 μm thick, hence the thickness of a full series of 148 immunostained sections covers the distance of more than 1 mm.

2. Classification of damaged sections

Before we can continue with the description of the registration and of the repair measures, we need to distinguish between different kinds of damage in the digitized serial sections. Fig. 3a shows a non-damaged section, stained for CD34, SMA, CD271. Possible damage includes:

1. A physically missing section. The section in total was lost during biological processing.
2. Damaged part of a section. Some region in the section sustained damage, that is visible in the image regardless the acquisition kind, see Fig. 3b.
3. A larger part of a section or whole section is not in focus. Short of repeated acquisition, nothing can be done for this section, see Fig. 3c.
4. Some region of a section is not in focus or damaged in a different manner; however, parts of a section are in focus and can be successfully used for the section-wide registration, compare Figs. 3d, 3e.

Boiled down to a ROI the above classification leads to two cases.

- An image in the series is irrecoverably lost and needs to be replaced.

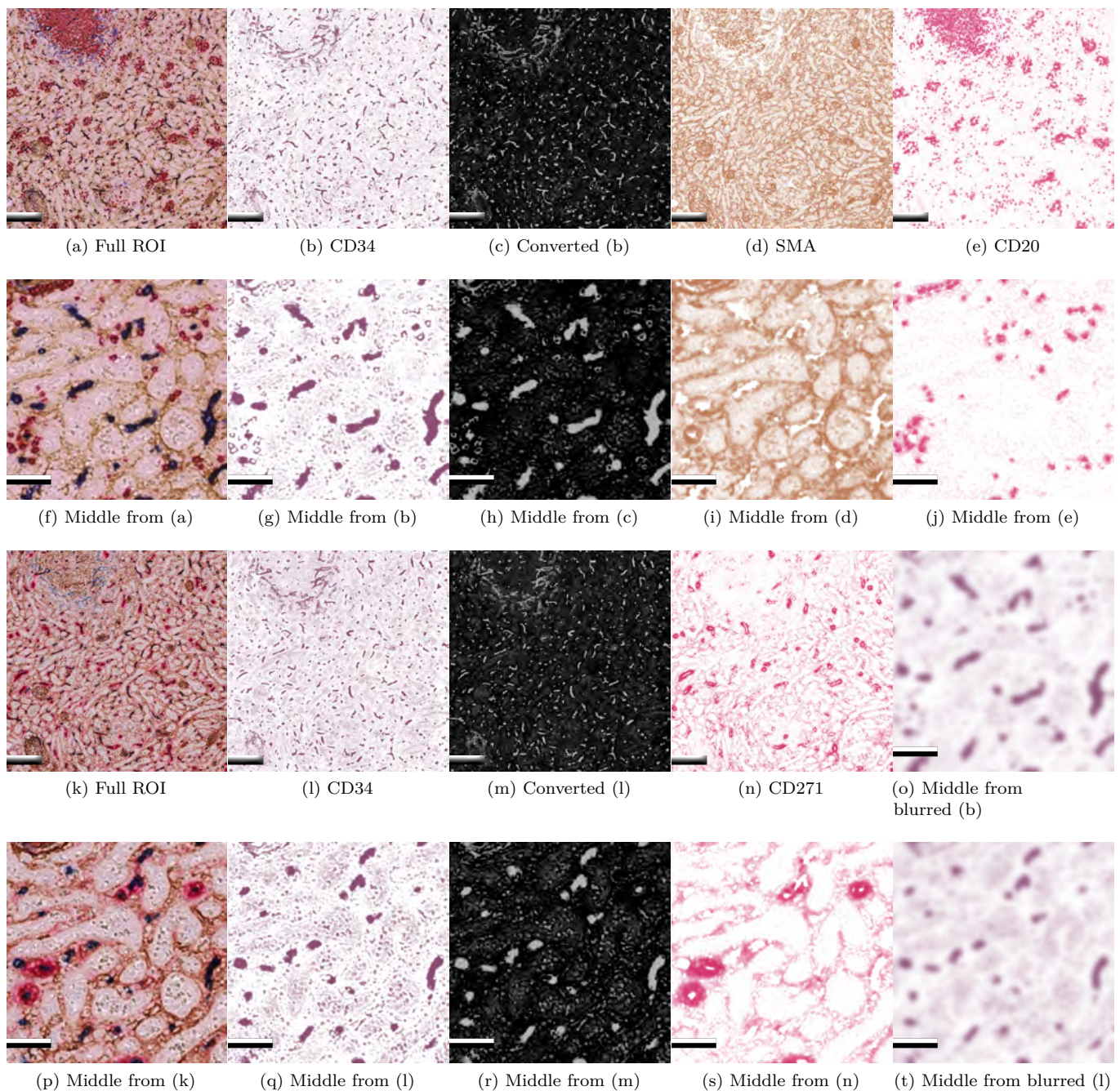


Figure 2: Overview of our main data set. The first and the third row show a $2.5k \times 2.5k$ pixels ROI, the second and fourth row zoom in at the center to show details. Subfigures (a)–(j), (o) show registered section no. 10 (even, with red for B-lymphocytes), subfigures (k)–(n), (p)–(t) show registered section no. 11 (odd, with red for capillary sheaths). In all cases, blue pigment is present in CD34-positive cells, brown in SMA-positive. Subfigures (o), (t) show zoomed blurred CD34 channel processed in the same way, the registration input is. Subfigures (c), (h), (m), (r) show the input channel for further processing. Scale bars for full images (first row and (k)–(n)) are $200\mu m$, scale bars for center crops (second, fourth rows and (o)) are $50\mu m$.

- A part of an image in the series is lost, but other parts are usable.

B. Processing

1. Registration of alternating series

The methods for the registration of different stainings are based on either human input or on some degree of similarity between the different modalities. Machine learning from the annotations of identical or similar objects in varying stainings is able to identify “common” labels that are, in their turn, registered to each other. In our case, we were not able to afford the luxury of manual labeling. A mutual information or an extended machine learning approach on the “extracted” CD34 channels appears viable, but we chose a different approach.

The biological experiment was designed to have some common stainings between two subseries, the CD34 and SMA channels. A known method to separate the different colors in a histological staining is color deconvolution [78]. We aimed to apply our previously developed registration method [68] to alternating series. This method is based on feature detection, matching, and non-rigid deformations. The latter were computed with a Krylov subspace optimization method [33]. For the actual deformations, B-splines were used. We decoupled the “detection” images (the images the registration works on) from the “transformation” images (the images the established transformations are applied to). We found it crucial to denoise the feature detection inputs using Gaussian blur with $\sigma = 6$ (see also Figs. 2o, 2t). Without blurring, we found it impossible to register the series. We speculate that the noise visible in Figs. 2g, 2q produced a lot of small, very similar features. These confused the non-rigid registration.

We obtained a registration of a full series in its original resolution (thousands of pixels per side). For it, we used a blur-based denoising; the registration was applied to the full sections (mitigating local problems); instead of the missing sections and of some damaged sections duplicates of their neighbors were used as a placeholder. The latter issue necessitates further processing.

A rigid phase and 4 levels on non-rigid deformations, were established on the blurred images and subsequently applied to the actual full series of complete sections. In our experiments we used the CD34 (blue) channel for the registration, as this channel contains continuous structures (blood vessels). Acquisition artifacts in the series also influenced the registration. We stress that above section replacements can be tolerated as an intermediate step only, as a missing section unequivocally means interruptions of the capillaries.

At this stage, a region of interest can be selected. In a typical 3D reconstruction pipeline we select ROIs of size

$2.5k \times 2.5k$ pixels for the final output of $2k \times 2k$ pixels after the final interpolation step.

2. Healing of separate channels

We used standard method by Reinhard et al. [89] as implemented by Khan et al. [53]. for the normalization of the ROIs.

The healing is commenced on normalized channel-separated images. First, a color deconvolution [78] is performed on the final registered images. We obtain four channels: CD34, SMA, CD271, and CD20. Color space conversion is performed from color-palettred 8-bit images (originating from color deconvolution) to intensity-based single-channel 8-bit images. To give an example, in Fig. 2 we converted the output of color deconvolution for CD34 (b), (l) to a negated green RGB channel (c), (m).

a. Healing in general We routinely use our optical-flow-based interpolation [67] to reduce the anisotropy of the data in our reconstructions [99, 101]. Having initially acquired the data with spatial resolution of $0.5 \mu\text{m}/\text{voxel} \times 0.5 \mu\text{m}/\text{voxel} \times 7 \mu\text{m}/\text{voxel}$, we produce volumes with $0.5 \mu\text{m}/\text{voxel} \times 0.5 \mu\text{m}/\text{voxel} \times 1 \mu\text{m}/\text{voxel}$ for the actual 3D reconstruction. We heavily modify this interpolation mechanism for the healing of missing sections.

Due to the nature of CD20 labeling (B-cells), we do not need to perform a “connecting” interpolation on it. SMA is rather used as a guide to distinguish larger arterioles from smaller capillaries; it can sustain some damage or replicated sections. CD271 appears only in every other section, so interpolation is needed here. We also apply the below method to CD271, but it is not as crucial there as it is for CD34. Repeated sections or missing image parts produce interruptions in blood vessels that are reconstructed from CD34 labeling. Such interruptions change the topology and connectivity of the blood vessel network. Hence, CD34 channel has to be healed.

b. Healing a completely missing image There is no “extra” information to come by, when an image is completely missing. Let us denote the image sequence in question with $A-X-B$. Image X is missing; images A and B are its neighbors. In some cases, to reduce the movement in the next step, we pairwise register A to B (yielding A') and B to A (yielding B') with *elastix* [55]. Notice that *elastix* is applied to already registered series. In other cases the movement can be bridged with optical flow, hence there we just set $A' := A$ and $B' := B$.

Next, we create an optical-flow-based intermediate images from A' to B' , resulting in the end with an image we call here X' . This way we aim to approximate the moving from A to X and from X to B in the whole series. The “movement” (originating from the registration and from the optical flow intermediates) is also of benefit for the 3D reconstruction, as it alleviates the artifacts from just mechanical replication of $A + B$ as purported X (cf. Table I and Fig. 8e). With it, some capillary connections

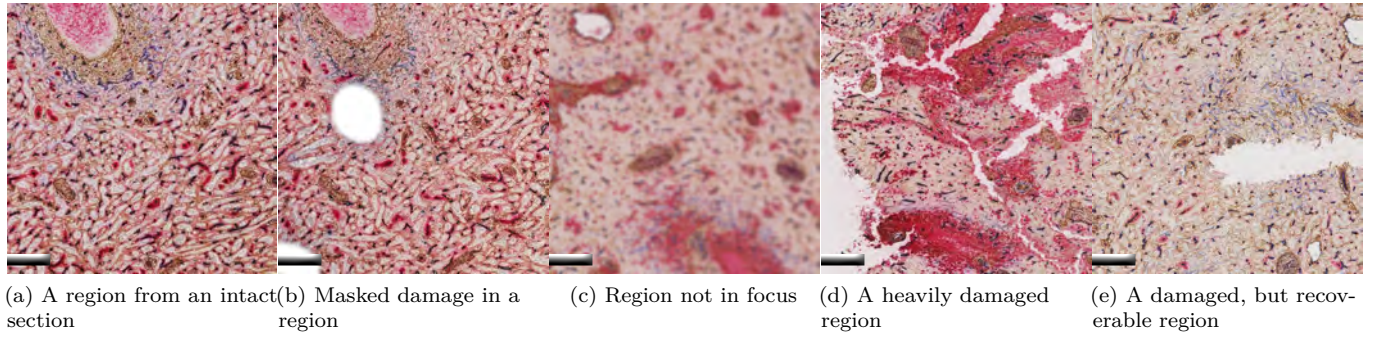


Figure 3: Examples for different kinds of damage in serial sections. All scale bars are 200 μm .

are maintained that would be broken otherwise (see also Fig. 9). Section II B 2 d details on optical flow and intermediates. The nature of the composition operator $+$ is a separate issue, see Section II B 2 e.

c. Healing missing parts of an image For the missing parts on an image the procedure is similar. Consider the same images A, X, B as above. However, as we now have a mask M on the damaged parts of the image X , instead of trying to “imagine” the whole contents of X , we need to do so only where M is not zero. The remaining, “valid” parts of X are mixed into the image X' . Also here the composition operator is important.

In the case of an out-of-focus image which is still marginally usable, the mask M is zero everywhere. The offending image is fittingly registered, because other regions outside of ROI are still in focus. In this case, adding it to the “imagined” image X' enhances the result, as Fig. 4 shows.

d. Optical flow and distortion Dense optical flow by Farnebäck [32] models signals f_1 and f_2 as quadrics, e.g., $f_1(x) = x^T A_1 x + b_1 x + c_1$, where A_1 is a symmetric matrix, b_1 is a vector, and c_1 is a scalar. The signal f_2 has a similar representation, it is displaced by d . Local polynomial approximations are used below. We simplify the notation by writing A for a local approximation $A(x)$.

Let $A := (A_1 + A_2)/2$ and $\Delta b := -(b_2 - b_1)/2$. The distance between f_1 and f_2 can be viewed as a displacement field d , depending on x , with $Ad = b$. Let

$$d(x) = \frac{\sum_I w A^T \Delta b}{\sum_I w A^T A}$$

with sums running over all x in a region I and $w(x)$ a weight for handling edges. In practice, the values $A^T A$, $A^T \Delta b$, $\Delta b^T \Delta b$ (for confidence) are computed point-wise. We use a multi-scale implementation from OpenCV [17, 50].

Let $\mathcal{D}(A, B)$ be the dense optical flow between matrices A and B . The flow is a vector field of local approximations $d(x)$. We denote by $\mathcal{F}_{A,B}^s(X)$ an operation than computes the flow $\mathcal{D}(A, B)$ and then distorts X by $s \cdot \mathcal{D}(A, B)$ for a scale factor $s \geq 0$. For example, $\mathcal{F}_{A,B}^{1/2}(A)$ distorts A halfway to appear similar to B . We utilize

OpenCV to apply the distortion.

e. Combining the flows for healing In both above cases of healing we compute the optical flow $\mathcal{D}(A', B')$ between A' and B' and also $\mathcal{D}(B', A')$. Then $\mathcal{D}(A', B')$ is used to distort A' at the magnitude s , with $0 \leq s \leq 1$, i.e., we compute $\mathcal{F}_{A',B'}^s(A')$. Similarly, we obtain the other direction $\mathcal{F}_{B',A'}^{1-s}(B')$. As we aim for a “middle ground”, we would combine $\mathcal{F}_{A',B'}^s(A')$ and $\mathcal{F}_{B',A'}^{1-s}(B')$ at $s = 1/2$. It is possible to use alpha-blending for the composition [67], but it is less useful here as Section III 3 reports. With alpha-blending, an intermediate is

$$\frac{1}{2} \mathcal{F}_{A,B}^{1/2}(A) + \frac{1}{2} \mathcal{F}_{B,A}^{1/2}(B).$$

Crucial for the good results is the proper composition mode. Here we primarily use “lighten”, i.e.,

$$Y = \mathcal{F}_{A,B}^{1/2}(A) \oplus \mathcal{F}_{B,A}^{1/2}(B),$$

where \oplus is the pixel-wise intensity maximum.

Finally, recall the presence of an image mask for healing only missing parts of an image. In this case, the non-masked parts of X are combined with the image Y with \oplus , resulting in the final result X' .

C. Further processing and visualization

After the healing, we interpolated the CD34, SMA, and CD271 volumes with our optical-flow-based method. The interpolated volumes were further processed in 3D Slicer [54, 85]—a bit differently for each channel. In case of CD34 (blood vessels), the volume processing consists of the morphological closing filter and Gaussian blurring. In some cases, e.g., for CD271, we also dilated the volumes. Then we generated the meshes [1, 7, 69] and processed them further [26, 49]. Section III 3 details on the mesh processing for this paper.

In practice, the final meshes were visualized in our virtual-reality-based application [66]. With the ability to place annotations and perform mesh painting, our software is used by the domain experts for knowledge discovery [99–101].

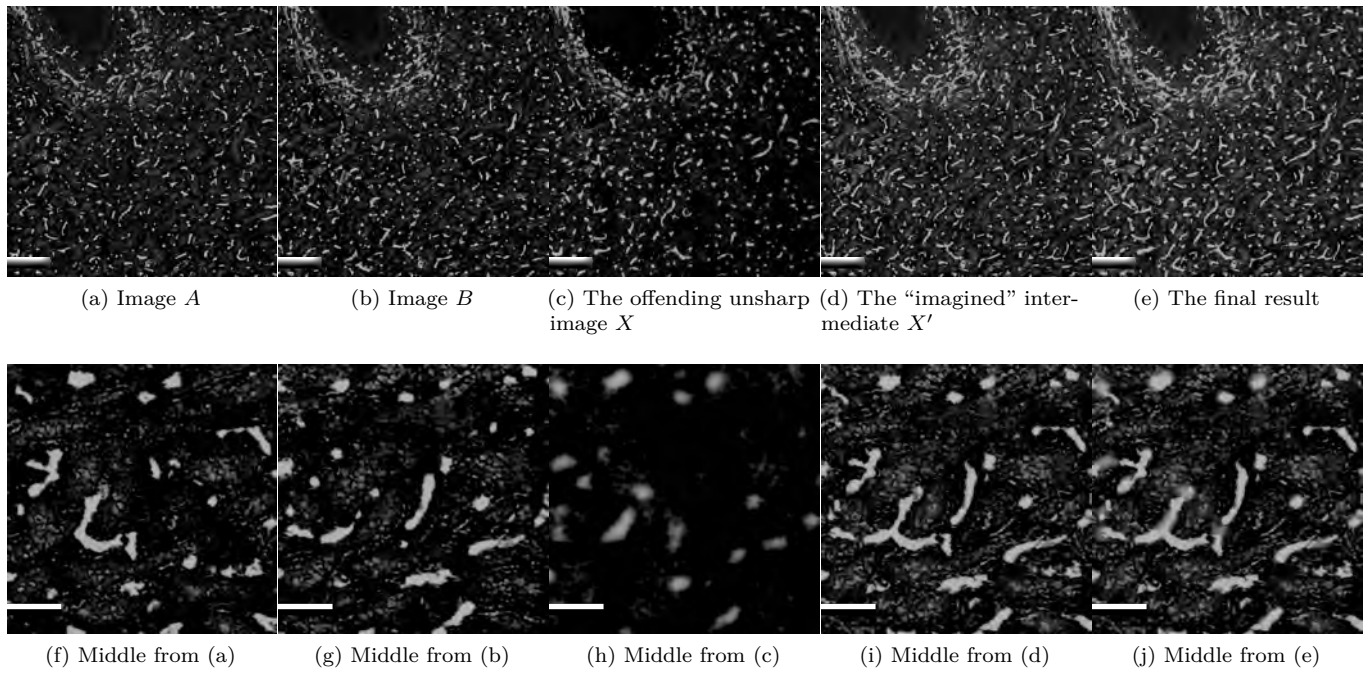


Figure 4: Healing an out-of-focus image. Still present information is reused. Scale bars in the top row are 200 μ m, scale bars in the bottom row are 50 μ m.

Table I: Numerical measures for the images from Fig. 6. The final result of our method is X' , i.e., Fig. 6b. The image Z is the result of our method on A and B , i.e., Fig. 6a. Basically, in the case of Z the registration is omitted. The images T and T' are the result of maximum intensity blending applied to the inputs A and B and to registered inputs A' and B' correspondingly. They basically omit the optical flow from our method. The Jaccard measure was computed on images with binary threshold 120. Values range between 0 and 1. The higher the values the better.

Image pair	SSIM	SSIM Figure	Jaccard
$A-B$	0.133	5c, 5g	0.123
$A'-B'$	0.0935	5k, 5o	0.0100
$A-A'$	0.159	—	0.0219
$Z-X'$	0.143	6c, 6g	0.359
$A-X'$	0.105	6i, 6m	0.238
$X'-B$	0.112	6j, 6n	0.251
$T-X'$	0.118	—	0.342
$T'-X'$	0.157	—	0.432
consecutive	0.185	—	0.285

III. RESULTS

With the presented method we were able to extend a consecutive series of 84 undamaged sections (Fig. 1a) to 148 sections spanning over a 1 mm in the direction of z axis (Fig. 1b). This means an grave 76.2% increase in

number of available images. Section III 3 details on how the both above images were reconstructed.

In general, medical experts rated our healed meshes higher than the alternatives and similar in quality to the truncated meshes. The rating was based on experts' perception of vasculature connectivity in ours reconstructions, which were inspected and quality controlled w.r.t. original registered sections in virtual reality. (Fig. 9 mimics such an analysis with geodesic distances.) Healing does not change intact images in the serial section stack. To quantify the difference between different methods, we use image- and mesh-based approaches below.

First, we evaluate our method with deformed and non-deformed input images, as well as compare the results of interpolation to the both neighbors in Section III 1. Sections III 2 a and III 2 b compare our healing method to ground truth on spleen and lung data sets. Section III 3 evaluates the 3D reconstructions from various healing strategies. The goal of this work was to restore broken connectivity in 3D reconstructions, hence it needs to be evaluated on those. All spleen images were normalized [89] to a common ground before processing.

1. Image-based evaluation of healing in production

Fig. 5 quantifies the elastix-based transformations of the input images. We compare original inputs A (a), (e) and B (b), (f) with A' (A registered to B) (i), (m) and B' (B registered to A) (j), (n) using SSIM (c), (g), (k), (o) and optical flow (d), (h), (l), (p).

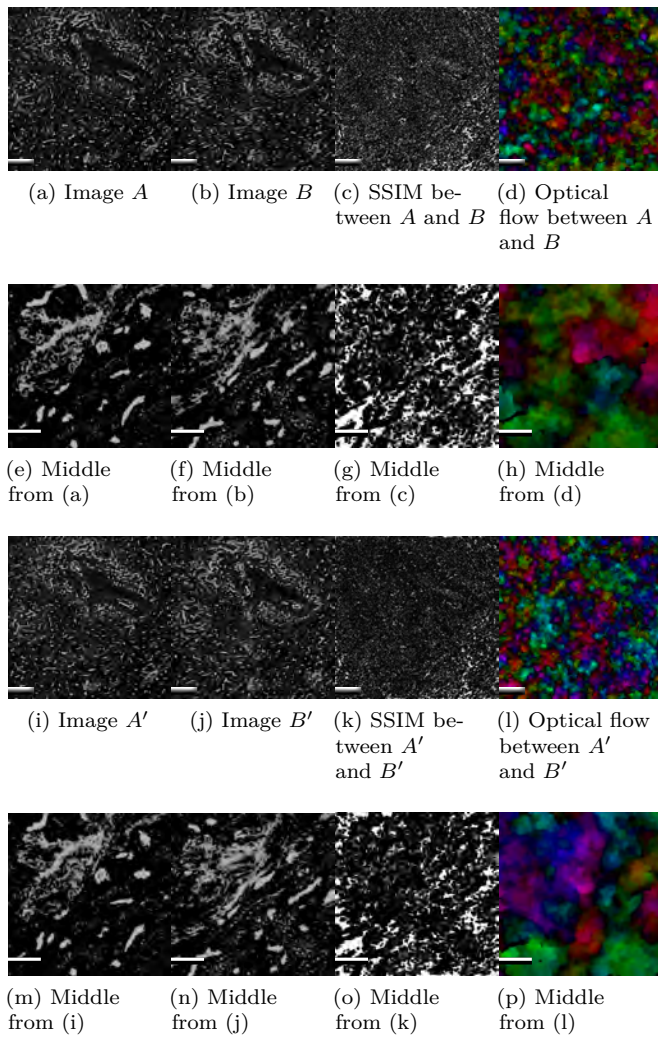


Figure 5: Normal and elastix-preregistered input for healing. Fig. 6 shows results. Table I presents SSIM and Jaccard values. Scale bars in the first and third rows are 200 μm , scale bars in the second and forth rows are 50 μm .

Fig. 6 showcases the results and quality measures of our method applied to the original inputs and to elastix-preregistered inputs. We see that SSIM is lower in $A'-X'$ (i), (m) and $X'-B'$ (j), (n) pairs than in $Z-X'$ pair (c), (g), where Z is the result of our method without prior registration (a). Jaccard measure (Table I) supports this statement and optical flow visualization shows some local movement in Fig. 6 (d), (h), (k), (l), (o), (p). Optical flow visualizations appear similar between $A-B$, and $A-X'$, $X'-B$ (Fig. 5, (l), (p), Fig. 6 (d), (h), (k), (l), (o), (p)), but consecutive sections yield less movement in optical flow (not shown). We argue that the local movement, shown to us by optical flow (k), (l), (o), (p), matches the desired outcome as we distort both images A and B to obtain a better intermediate.

In Table I the differences in SSIM and Jaccard measure

Table II: Evaluating our method with ground truth on a spleen data set (Fig. 7). Image A precedes the actual interpolated image, image X is the ground truth, image X' is the interpolated image. Values range between 0 and 1. The higher the values the better.

Image pair	SSIM	Jaccard
$A-X$	0.151	0.289
$A-X'$	0.182	0.354
$X-X'$	0.125	0.346

are similar between $A-X'$, $X'-B$ and two consecutive sections. Surprisingly, both SSIM and Jaccard measure are very low for $A'-B'$ pair (Fig. 5k), i.e., for repeatedly registered input. A possible explanation is that A' is distorted to fit B , but B' is distorted to fit A . It is rather a way to distort both images towards an unavailable common ground X than a proper registration of A to B .

The highest Jaccard value results from an image pair $T'-X'$. Images T and T' apply the blending method of our choice \oplus to original (basically, $T = A \oplus B$) and registered images ($T' = A' \oplus B'$). Still, there is a substantial difference between T' and X' . Similarly, there is a difference between X' and Z (our method applied to A and B), resulting from repeated registration. Notice that our optical-flow-based interpolation also introduces local distortions.

2. Evaluation of healing on known images

a. Spleen We took three undamaged consecutive sections from our main data set, cropped them to $2.3k \times 2.3k$ pixels for more clarity, and pretended that the middle section needs to be healed. Full image was to be healed. We then subsequently computed the image measures similar to the previous section. No additional registration of images A and B was used. Fig. 7 and Table II report on our findings. The pair $A-X$ is consecutive. SSIM between X and X' (j), (n) appears lower (i.e., worse) than between A and X' (i), (m). Optical flow visualizations are inconclusive in (l), (p) vs. (k), (o), but all those visualizations have some bright spots. Jaccard measure is slightly lower for $X-X'$. Summarizing, SSIM is higher at $A-X'$ pair, as X' partially consists of A . In a contrast, Jaccard measure is similar between $A-X'$ and $X-X'$, the relatively high latter value allows us to rate the healing result as a success. Still, we evaluate also the models with different healing methods in Section III 3.

b. Lung To demonstrate that our method works also on very different sections, we took a subseries of a rat lung serial sections [37, 38, 98]. Specifically, 2604 semi-thin sections with thickness of 1 μm of a pathological lung from a 12 week old Fischer F344 male rat were produced. The sections were stained with toluidine blue. A short resampled subseries with 800×800 pixels was

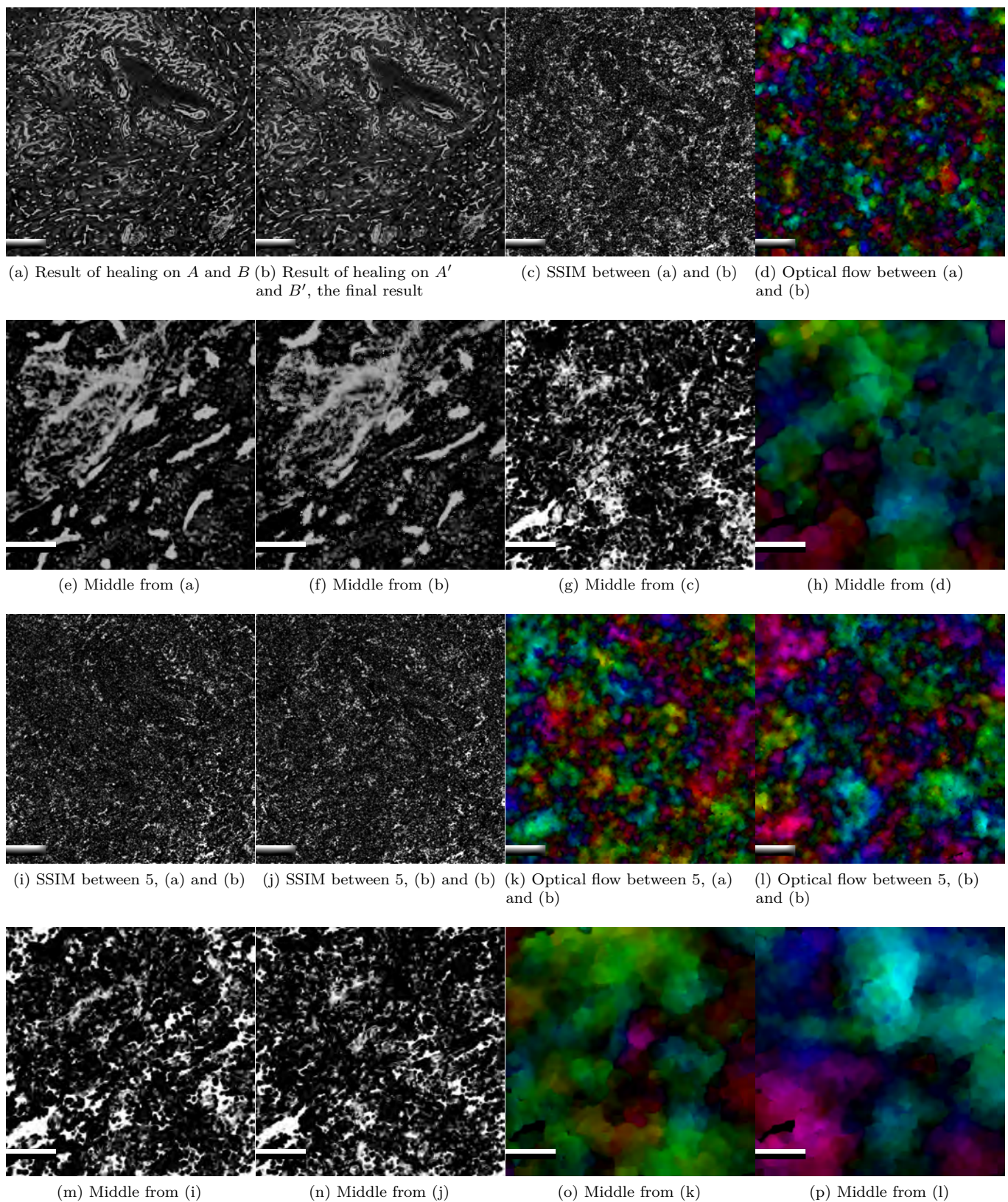


Figure 6: Healing in a case with elastix-preregistered input. Quantification of input images is in Fig. 5. See Table I for SSIM and Jaccard values. In SSIM, the brighter are the images, the better. In optical flow, the darker the images are, the better. Scale bars in the first and third rows are 200 μm , scale bars in the second and forth rows are 50 μm .

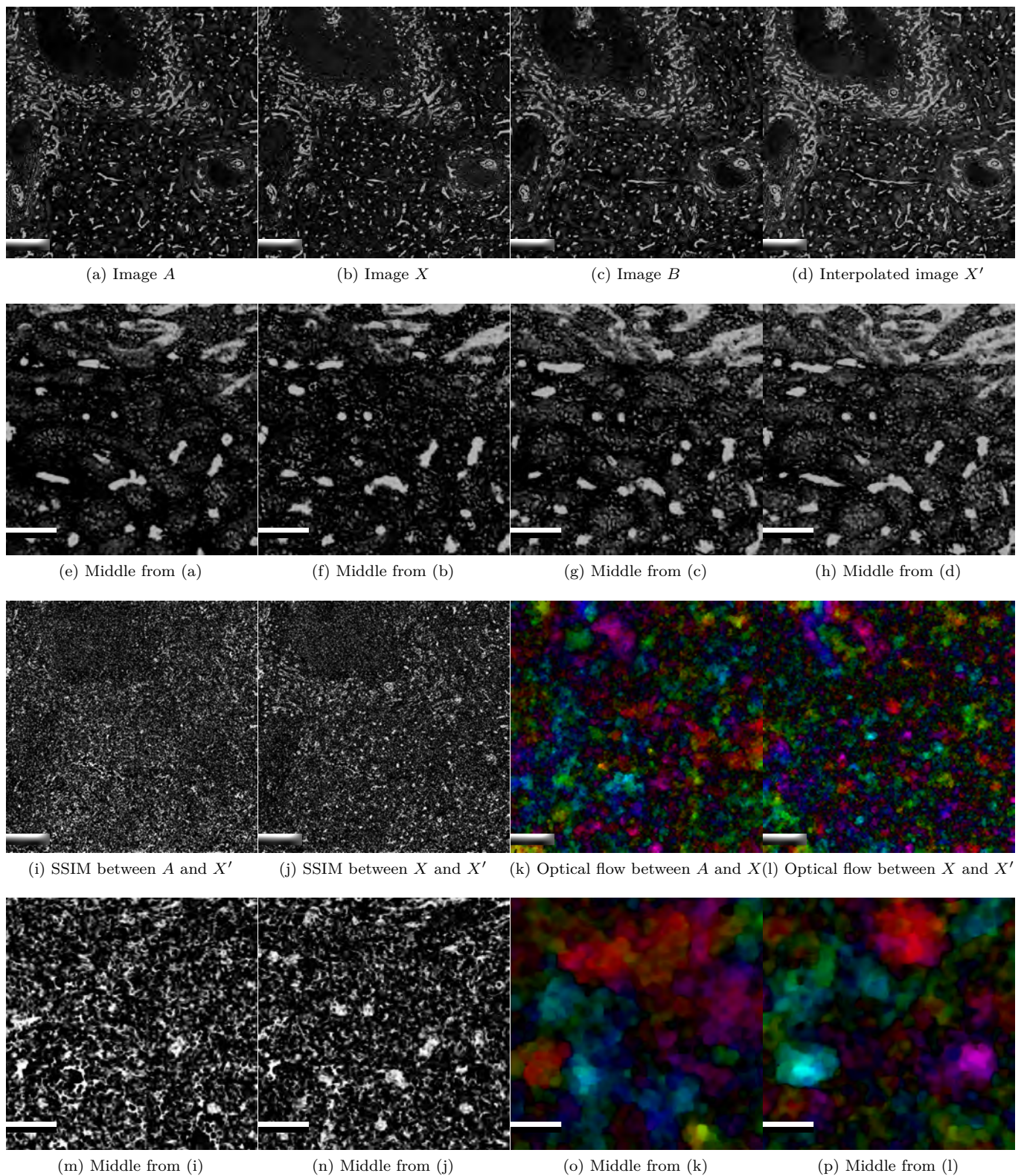


Figure 7: Evaluating our method with ground truth on a spleen data set. Image (b) is the ground truth, image (d) is the result of our method. In SSIM, the brighter are the images, the better. In optical flow, the darker the images are, the better. Scale bars in the first and third rows are 200 μm , scale bars in the second and forth rows are 50 μm .

selected for testing. It was rigidly pre-registered using our usual registration [68]. Images A and B were non-rigidly registered towards each other with elastix [55], resulting in A' (a) and B' (c). The images presented here were cropped after processing to 500×500 pixels to omit edge effects from registration. We did not apply normalization.

Fig. 8 shows the evaluation of our method on lung data with ground truth. SSIM and optical flow were computed on the full images, optical flow signaled larger changes at image edges. We show 500×500 center crops from those quality measures in Figs. (g), (h). SSIM between the ground truth X (b) and interpolated image X' (d) on the full images, including the non-matching edges, is 0.846, SSIM between same cropped images is 0.935. We interpret this very high SSIM value as a success. Low values of the optical flow in Fig. 8h support this interpretation.

3. Evaluation of final 3D models

To evaluate different approaches, we use nearest neighbor interpolation (a straightforward approach), truncate series to contain only “good” sections, utilize an optical-flow-based interpolation with alpha-blending (our method with blending per [67]), and use the method presented here, optical-flow-based interpolation with intensity-maximum-blending. All these methods are applied to the same spleen image series.

In all cases, the full 3D reconstruction pipeline is utilized. We start with a registered data set [68], apply normalization [89], color deconvolution [78], and above healing methods. After healing, inter-slice interpolation [67] is applied, followed by volume filtering. We apply 3D grayscale closing filter with radius 7 and a Gaussian blur with $\sigma = 1$. Then, the mesh is constructed with iso-value 120. We apply mesh repair [49] (octree depth 9), Taubin smoothing [103], and small component removal (at 2% of the main diagonal). Figure 1 visually compares the cropped and healed meshes. We then compute geodesic distances from the same starting point and over the distance of 100% of the main diagonal.

Figure 9 compares the features of the three complete meshes. The data sets are very dense and self-occluding. The difference between the methods is visible in the amount of connections in the blood vessels. In other words, where more interruptions are (due to missing or non-present repair), there more unconnected components ensue. Such components are colored in dark red.

If we zoom in (Figs. 9d–9l), we see some not-connected blood vessels in dark red in nearest neighbors and in alpha-blended meshes. Those blood vessels are connected with our method. To be more specific, some blood vessels were not connected with nearest neighbors (d), (g), or with optical-flow-based healing with alpha blending (k). Those blood vessels were connected when using optical-flow-based healing with maximum blending (f), (l). Supplementary video shows the mesh from (c) in motion.

We additionally evaluated all the vertices in those four

meshes by their connectivity with above geodesic distance computation. Fig. 10 considers a) number of vertices having the geodesic distance of zero (i.e., not connected to the starting point) compared to the number of connected vertices; b) the violin plot [43] of geodesic distances for all vertices in each of the meshes. It appears hard to describe the differences between the reconstructions statistically.

IV. DISCUSSION AND FUTURE WORK

1. Existing methods

a. Registration Registration methods typically assume a certain degree of similarity in the representation between the to-be-registered images. Focusing on registration of serial sections, in most cases the staining the same throughout the series (“unimodal” registration). In a classical multimodal registration the subject is the same, but the representations (i.e., the stainings) are different. A “common ground” needs either to be established with a segmentation, or similarities are established with a machine learning method. Basically, an intermediate representation, similar for all modalities is established. The registration operates on this intermediate, the actual transformations are then transferred to the original images.

In our case, the registration of an alternating series is a typical research task. Our stainings are established to answer a research question. This is a very different setting from establishing a multimodal registration for routine clinical stainings. Clinical stainings will be created in larger amounts for years after the establishing the registration. Hence, a machine learning approach makes economically sense, even with some additional manual labeling to bootstrap the learning. In our case, there are too many sections to be labeled by hand and too few to establish a proper machine learning method. Per design of the biological study, we have, however, a “common ground” in form of SMA and CD34 stainings in our data.

We previously used CD34 to establish a registration of uniformly stained serial sections. In the case of the registration of alternating series, the pure CD34 channel extraction by the means of color deconvolution did not work, but a denoised CD34 channel performed well.

Thus, we present here not an unconditional multimodal registration method that can operate on sections with no common ground via some similarity measure, but a fully automatic method to lift a registration method from uniform stainings to alternating stainings with a common ground.

Our contribution is thus different from all known to us related work on “unimodal” and multimodal registration. It is a very technical, but decisive and new contribution that allows for all the further processing in the 3D reconstruction pipeline. Our experience might be useful for others when designing a study with more channels than chromogens usable at once. We basically show the way

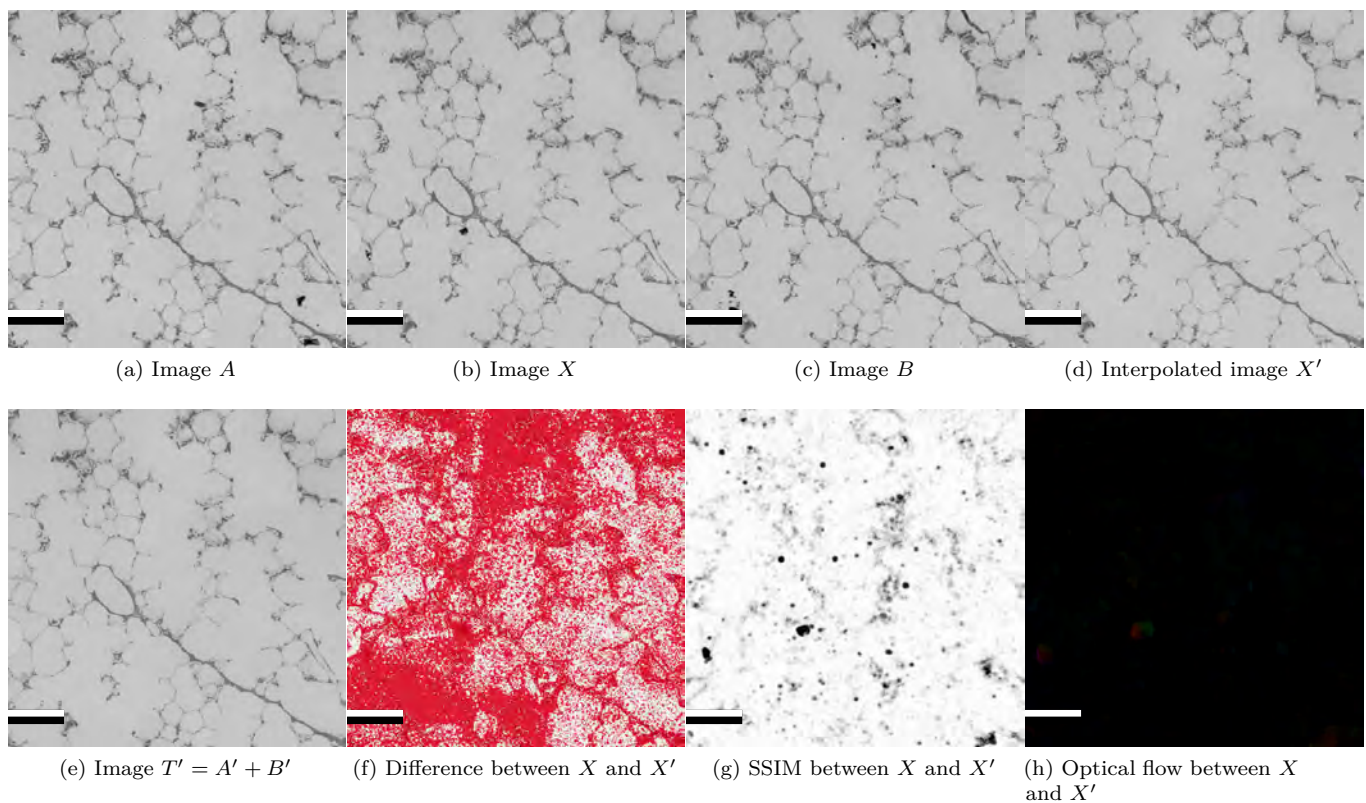


Figure 8: Evaluating our method with ground truth on a lung data set. Images A (a) and B (c) are used as an input. Image X (b) is the ground truth, image X' (d) is the result of our method. Image T' (e) is a direct combination of A' and B' using maximum composition. Fig. (f) shows more than 1% difference between X and X' in red. In SSIM (g), the brighter are the images, the better. In optical flow (h), the darker the images are, the better. All scale bars are 200 μm .

for a conventional, “unimodal” registration (in our case: a fully automatic feature-based method) to “survive” an alternating stainings. The prerequisite is that some ubiquitous structures are present in both stainings, labeled in the same manner. Nerves or blood vessels are examples of such structures.

b. “Healing” In the biomedical community a damaged histological section is often perceived as an inevitable artifact of lab work. Such artifacts are seldom reported in publications; basically a further, better section is to be produced to make the result publishable. This behavior is, however, not quite productive in 3D reconstructions from serial sections. A series needs to be consecutive for a 3D reconstruction. Should a section in the middle of a series be missing, only truncating a series or repair approaches are viable. A typical approach of others is to “repeat” the nearest neighbor section. Fig. 9 (d), (g) shows the drawbacks of this approach in form of broken connectivity in dark red.

All prior repair methods known to us cannot deal with damaged sections without losing the connectivity of microvessels. Our method is able to maintain such a connectivity, which is novel.

In ref. [97] missing sections are reported to degrade the quality of registration. Our registration is able to bridge a missing section by repeating a neighbor. However, we had to introduce the presented method to maintain blood vessel connectivity. Burton et al. [21] have averaged nearest neighbor sections. We show that our method is more precise than the nearest neighbor repetition or even than the “healing” with alpha-blending (Fig. 9). Our method involves further non-linear distortions stemming from additional registration beforehand and from transformations induced by optical flow. Such non-linearity contrasts our approach with averaging. Our method is also more reproducible than sketching the missing sections from low-resolution unstained overview [91].

It appears to be viable to “heal” a missing section with existing mechanisms for the interpolation between sections [22, 67]. Indeed, we also used optical flow for such interpolations. However, we found that a correct blending method is crucial for the success of section repair, as Fig. 9k shows.

Summarizing, our method is more sophisticated and more precise in maintaining connectivity than other approaches. Our method is also more reproducible than the

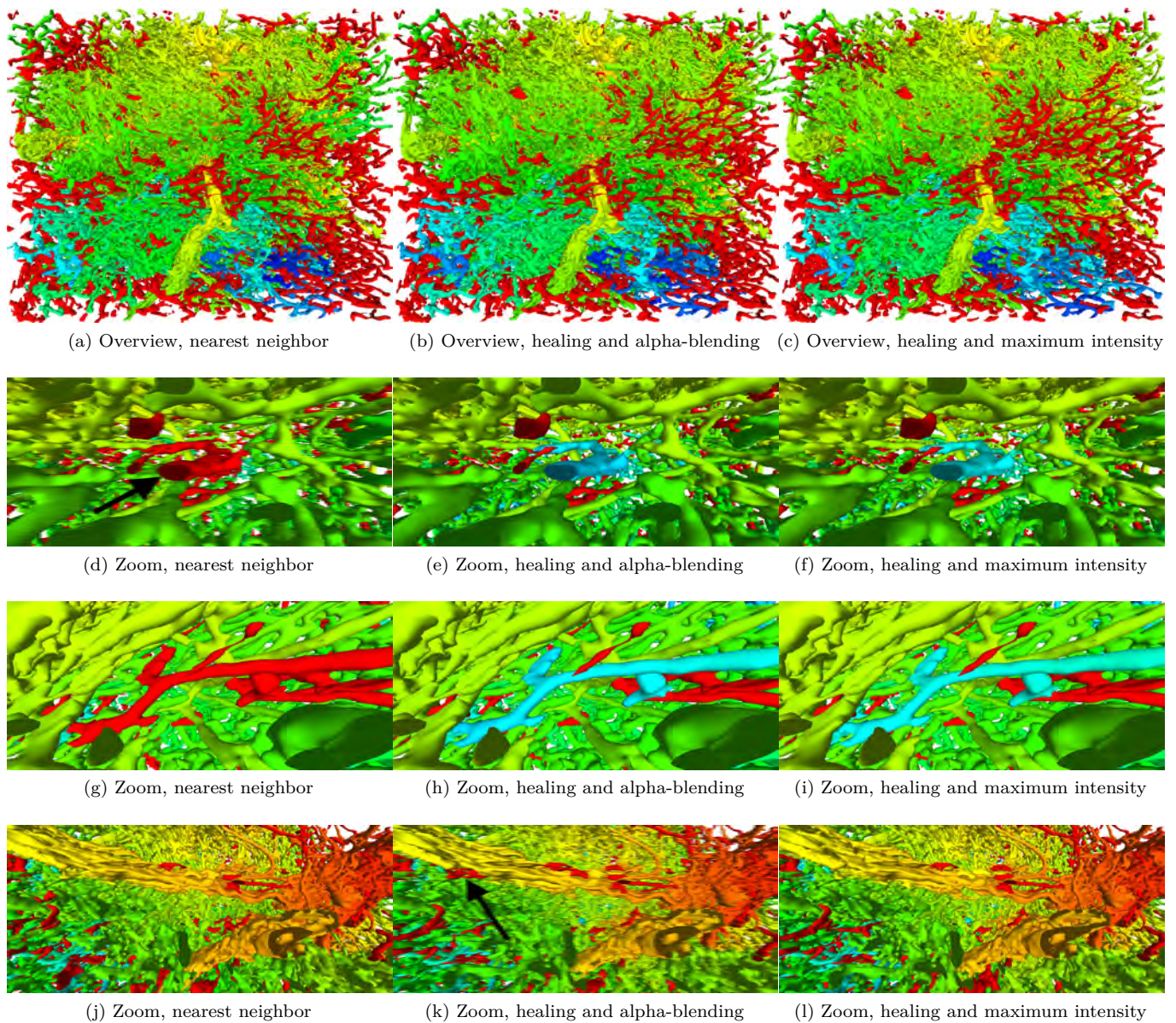


Figure 9: Geodesic distances from same origin for different kinds of healing applied to the same data set. Notice unconnected parts of blood vessels in dark red in other healing methods, marked with black arrows. Figs. (a)–(c) provide an overview, (d)–(l) show detailed views. The widths of the complete reconstructions (a)–(c) are 1 mm each.

suggestions from the literature.

2. Evaluation criteria

It appears hard to us to precisely and practically evaluate the connectivity of the data in a very large, highly self-occluding data set. Using synthetic data can be an option, but real data sets are much more complex and might leave some cases unhandled in mock data. Image-based metrics (Tables I, II) show rather the correspondence of

two images, whereas a good healing “imagines” a middle ground between two images. We found empirically that distorting the two neighbor images and then combining them to an intermediate produces better results, but this approach naturally slightly decreases the similarity between the intermediate and original neighbor images. It also appears that the repeated registration to A' and B' decreases the similarity between both distorted images as well. This is not bad as such, as long as the optical flow has enough common ground to perform well. Statistic evaluations (Fig. 10) of whole meshes are quite subdued: some broken-off parts might be a very minor issue statistically,

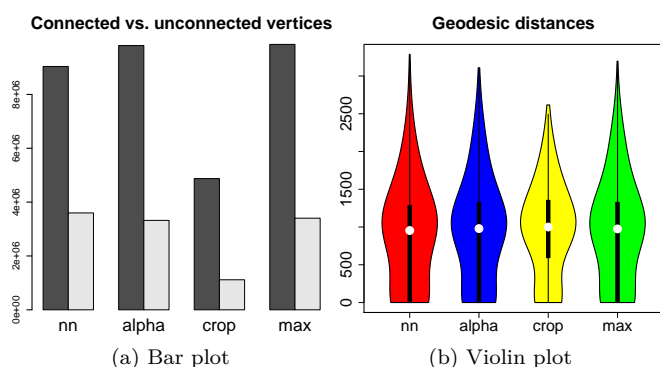


Figure 10: Statistical evaluation of reconstructed meshes. In (a), the dark bars show the number of connected vertices (the higher, the better), the light bars show the number of unconnected vertices (the lower, the better). The violin plots in (b) show the general distribution of the geodesic distances on all vertices. In both figures, “nn” stands for nearest neighbor, “alpha” for our healing method with alpha blending, “crop” for the truncated volume with no damaged sections, “max” for our healing method with maximum blending.

but it would be appallingly clear during a visualization or a visual analytics session.

For the above reasons we regard a mesh-based evaluation of the repair methods crucial. In Fig. 9 we found some branches not connected in alternative methods that are connected in our suggested approach. A proper quality metric is also relevant in the context of the next section.

3. Deep learning

Image-based deep learning methods for recovery of missing image parts, e.g., ref. [115], are relevant and can be used to extend this work. Even more interesting are mesh- or voxel-based deep learning methods [16, 40, 47, 62, 88, 95, 114] with which a similar task to our original motivation could also be solved: interruptions in a 3D scene due to missing data could be detected, classified, and repaired. We further discuss this idea in the next section.

However, the big questions on the reproducibility of the results and on understanding of the actions of the network might hinder wider adoption of a deep-learning-based method in the area of medical imaging. Our healing method has a nice property of being a combination well-understood image transformations. Should a mistake in our method be detected, the source of the problem can be found easily.

Quality control criteria for connectivity repairs are quite easily defined. Corner cases are: something is not connected, but it should be; something is connected, but should not be.

4. Future work

Further adjustments of the registration technique are viable. These include experiments with further feature detection, description, and matching algorithms. An extension of matching to incorporate the structure of the data set could further improve the registration. Offloading more work to the GPU would improve execution times.

In general, registration methods for larger alternately-stained sections would be always sought for. The reason for this is that immunohistochemistry for transmitted light microscopy (and also, but less so, for fluorescence) is limited in the number of simultaneous “channels”, the number of antibodies that can be combined in a single staining.

Of course, we look forward to apply our healing technique to further series and organs. Optical microscopy images from serial semi-thin sections of animal lung probes look promising; Section III 2b showcases our first attempts. A more confident investigation of human bone marrow stainings for blood vessels and certain progenitor cells becomes more viable. A healing technique becomes even more crucial in the context of larger human tonsil data sets, as this organ is often damaged during acquisition.

It still appears interesting to straightforwardly apply deep learning to image-based healing and to compare the result with our method. This study does not use machine learning methods by its design, as it aims for explainable intermediates. Future voxel- or mesh-based healing methods (potentially based on works mentioned above) might be instrumental in correction of the interruptions in biological mesh data.

V. CONCLUSIONS

The contributions of this paper are twofold. Firstly, we found a way of registering alternating histological serial sections using an originally non-multimodal registration method. Secondly, we present a methodology to repair damaged or missing sections from a histological series.

With a simple, but previously not published trick, we registered a series of alternating serial sections, 148 images with dozens of thousands pixels per side. Our approach is based on color deconvolution and image filtering, followed by an existing feature-based registration. Our method is fully automatic. Basically, we have “lifted” a registration method that operated on a series with same stainings to a method operating on alternating series.

Damage happens routinely at all phases of processing serial sections, during biological processing, during acquisition, or even during digital processing—registration errors, for example. We were able to “heal” missing data from a series of sections. We reached our goal of recovering the lost 3D connectivity in a histological series with image-based methods. Our healing methodology promises the availability of larger series and larger potential 3D

reconstructions, which facilitates better understanding of biological structures.

Specifically, applying the presented methods to a series of 148 immunostained serial sections, we were able to reconstruct more than 1 mm³ of a tissue at a microscopic resolution. In the same region only 84 sections could have been reconstructed with conventional methods.

VI. ACKNOWLEDGMENT

The author is thankful to B. S. Steiniger (Philipps-University of Marburg) for the awesome possibility to work with digitized biological data that led him closer to the life sciences. Most of the biological data shown in this work originates from her lab. M. Guthe (University of Bayreuth) provided hardware, software, and his support. C. Mühlfeld (Hannover Medical School) supported the

author with a position at the Hannover Medical School. A. Seiler, K. Lampp, and H. Pfeffer (Philipps-University of Marburg) were involved in the preparation and processing of the spleen serial sections. We thank A. Schauss (University of Cologne) for the acquisition of the spleen data. The author thanks R. Grothausmann, L. Knudsen, C. Mühlfeld (Hannover Medical School) and M. Ochs (currently Charité Berlin) for the availability of the lung data. S. Faßbender (Hannover Medical School) prepared the lung serial sections. M. Berthold (currently BCM Solutions GmbH) was involved in software development of the renderer used in the video. We used SSIM implementation by R. Mehdi.

This work was supported in part by German Research Foundation (DFG) grant no. 420759458. A part of this work was performed while the author was still at the University of Bayreuth.

- [1] James Ahrens, Berk Geveci, and Charles Law. *Paraview: An end-user tool for large data visualization*. Elsevier. ISBN 978-0-1238-7582-2.
- [2] Lejla Alic, Joost C. Haeck, Stefan Klein, Karin Bol, Sandra T. van Tiel, Piotr A. Wielopolski, Magda Bijster, Wiro J. Niessen, Monique Bernsen, Jifke F. Veenland, and Marion de Jong. Multi-modal image registration: matching MRI with histology. In *Medical Imaging 2010: Biomedical Applications in Molecular, Structural, and Functional Imaging*, volume 7626, page 762603. SPIE. doi: 10.1117/12.844123.
- [3] Najah Alsubaie, Nicholas Trahearn, Shan E. Ahmed Raza, David Snead, and Nasir M. Rajpoot. Stain deconvolution using statistical analysis of multi-resolution stain colour representation. *PLOS ONE*, 12(1):e0169875. ISSN 1932-6203. doi: 10.1371/journal.pone.0169875.
- [4] Fouzia Altaf, Syed M. S. Islam, Naveed Akhtar, and Naeem K. Janjua. Going deep in medical image analysis: Concepts, methods, challenges and future directions. *arXiv:1902.05655 [cs]*. URL <http://arxiv.org/abs/1902.05655>.
- [5] J. L. Andersson, A. Sundin, and S. Valind. A method for coregistration of PET and MR brain images. *J. Nucl. Med.*, 36(7):1307–1315. ISSN 0161-5505.
- [6] J Ashburner and K Friston. Multimodal image coregistration and partitioning—a unified framework. *NeuroImage*, 6(3):209–217. ISSN 1053-8119. doi: 10.1006/nimg.1997.0290.
- [7] Utkarsh Ayachit. *The Paraview guide: A parallel visualization application*. Kitware, Inc. ISBN 978-1-9309-3430-6.
- [8] Chiara Bagattini, Tuomas P. Mutanen, Claudia Fracassi, Rosa Manenti, Maria Cotelli, Risto J. Ilmoniemi, Carlo Miniussi, and Marta Bortoletto. Predicting Alzheimer’s disease severity by means of TMS–EEG coregistration. *Neurobiol. Aging*, 80:38–45. ISSN 0197-4580. doi: 10.1016/j.neurobiolaging.2019.04.008.
- [9] Simon Baker, Daniel Scharstein, J. P. Lewis, Stefan Roth, Michael J. Black, and Richard Szeliski. A database and evaluation methodology for optical flow. *International Journal of Computer Vision*, 92(1):1–31. ISSN 0920-5691, 1573-1405. doi: 10.1007/s11263-010-0390-2.
- [10] Guha Balakrishnan, Amy Zhao, Mert R. Sabuncu, Adrian V. Dalca, and John Guttag. An unsupervised learning model for deformable medical image registration. In *2018 IEEE/CVF Conference on Computer Vision and Pattern Recognition*, pages 9252–9260. IEEE. ISBN 978-1-5386-6420-9. doi: 10.1109/CVPR.2018.00964.
- [11] Serdar K. Balci, Polina Golland, Martha Elizabeth Shenton, and William Mercer Wells. Free-form B-spline deformation model for groupwise registration. *Med Image Comput Comput Assist Interv*. doi: 10.1901/jaba.2007.10-23.
- [12] É. Bardinet, S. Ourselin, D. Dormont, G. Malandain, D. Tandé, K. Parain, N. Ayache, and J. Yelnik. Co-registration of histological, optical and MR data of the human brain. In Takeyoshi Dohi and Ron Kikinis, editors, *Medical Image Computing and Computer-Assisted Intervention — MICCAI 2002*, LNCS, pages 548–555. Berlin Heidelberg. Springer. ISBN 978-3-540-45786-2. doi: 10.1007/3-540-45786-0_68.
- [13] Kathrin Becker, Martin Stauber, Frank Schwarz, and Tim Beißbarth. Automated 3d–2d registration of x-ray microcomputed tomography with histological sections for dental implants in bone using chamfer matching and simulated annealing. *Comput. Med. Imag. Grap.*, 44: 62–68. ISSN 08956111. doi: 10.1016/j.compmedimag.2015.04.005.
- [14] Kanwal K. Bhatia, Jo Hajnal, Alexander Hammers, and Daniel Rueckert. Similarity metrics for groupwise non-rigid registration. In Nicholas Ayache, Sébastien Ourselin, and Anthony Maeder, editors, *Medical Image Computing and Computer-Assisted Intervention – MICCAI 2007*, LNCS, pages 544–552. Springer. ISBN 978-3-540-75759-7. doi: 10.1007/978-3-540-75759-7_66.
- [15] K.K. Bhatia, J.V. Hajnal, B.K. Puri, A.D. Edwards, and D. Rueckert. Consistent groupwise non-rigid registration for atlas construction. In *2004 2nd IEEE International Symposium on Biomedical Imaging: Nano*

- to Macro (*IEEE Cat No. 04EX821*), pages 908–911 Vol. 1, . doi: 10.1109/ISBI.2004.1398686.
- [16] Davide Boscaini, Jonathan Masci, Emanuele Rodolà, and Michael Bronstein. Learning shape correspondence with anisotropic convolutional neural networks. volume 29 of *Advances in Neural Information Processing Systems*, pages 3189–3197. Curran Associates, Inc.
 - [17] G. Bradski. The OpenCV library. *Dr. Dobb's Journal of Software Tools*.
 - [18] U.-D. Braumann, N. Scherf, J. Eienkel, L.-C. Horn, N. Wentzensen, M. Loeffler, and J.-P. Kuska. Large histological serial sections for computational tissue volume reconstruction. *Methods Inf. Med.*, 46(5):614–622, . ISSN 0026-1270, 2511-705X. doi: 10.1160/ME9065.
 - [19] Ulf-Dietrich Braumann, Jens Eienkel, Lars-Christian Horn, Jens-Peer Kuska, Markus Löffler, Nico Scherf, and Nicolas Wentzensen. Registration of histologic colour images of different staining. In Heinz Handels, Jan Ehrhardt, Alexander Horsch, Hans-Peter Meinzer, and Thomas Tolxdorff, editors, *Bildverarbeitung für die Medizin 2006*, Informatik aktuell, pages 231–235, Berlin Heidelberg, . Springer. ISBN 978-3-540-32137-8. doi: 10.1007/3-540-32137-3_47.
 - [20] D. Bug, S. Schneider, A. Grote, E. Oswald, F. Feuerhake, J. Schüler, and D. Merhof. Context-based normalization of histological stains using deep convolutional features. In M. Jorge Cardoso, Tal Arbel, Gustavo Carneiro, Tanveer Syeda-Mahmood, João Manuel R.S. Tavares, Mehdi Moradi, Andrew Bradley, Hayit Greenspan, João Paulo Papa, Anant Madabhushi, Jacinto C. Nascimento, Jaime S. Cardoso, Vasileios Belagiannis, and Zhi Lu, editors, *Deep Learning in Medical Image Analysis and Multimodal Learning for Clinical Decision Support*, volume 10553 of *LNCS*, pages 135–142. Springer. ISBN 978-3-319-67558-9. doi: 10.1007/978-3-319-67558-9_16.
 - [21] Rebecca A. B. Burton, Peter Lee, Ramón Casero, Alan Garny, Urszula Siedlecka, Jürgen E. Schneider, Peter Kohl, and Vicente Grau. Three-dimensional histology: tools and application to quantitative assessment of cell-type distribution in rabbit heart. *Europace*, 16:iv86–iv95, November 2014. ISSN 1099-5129. doi: 10.1093/europace/euu234.
 - [22] Lucian Carata, Dan Shao, Markus Hadwiger, and Edward Groeller. Improving the visualization of electron-microscopy data through optical flow interpolation. In *Proceedings of the 27th Spring Conference on Computer Graphics, SCCG '11*, pages 103–110. ACM. ISBN 978-1-4503-1978-2. doi: 10.1145/2461217.2461238.
 - [23] Kenny H. Cha, Lubomir Hadjiiski, Ravi K. Samala, Heang-Ping Chan, Elaine M. Caoili, and Richard H. Cohan. Urinary bladder segmentation in CT urography using deep-learning convolutional neural network and level sets. *Med. Phys.*, 43(4):1882–1896. ISSN 2473-4209. doi: 10.1118/1.4944498.
 - [24] Liang-Chieh Chen, George Papandreou, Iasonas Kokkinos, Kevin Murphy, and Alan L. Yuille. DeepLab: Semantic image segmentation with deep convolutional nets, atrous convolution, and fully connected CRFs. 40:834–848, April 2018. doi: 10.1109/TPAMI.2017.2699184.
 - [25] Xi Cheng, Li Zhang, and Yefeng Zheng. Deep similarity learning for multimodal medical images. *Comput. Methods Biomech. Biomed. Engin.*, 6(3):248–252. ISSN 2168-1163. doi: 10.1080/21681163.2015.1135299. 1st MICCAI workshop on Deep Learning in Medical Image.
 - [26] P Cignoni, M Callieri, M Corsini, M Dellepiane, F Ganovelli, and G Ranzuglia. MeshLab: an open-source mesh processing tool. In *Eurographics Italian chapter conference*, pages 129–136, July 2008.
 - [27] Adrian V. Dalca, Guha Balakrishnan, John Guttag, and Mert R. Sabuncu. Unsupervised learning for fast probabilistic diffeomorphic registration. In Alejandro F. Frangi, Julia A. Schnabel, Christos Davatzikos, Carlos Alberola-López, and Gabor Fichtinger, editors, *Medical Image Computing and Computer Assisted Intervention – MICCAI 2018*, volume 11070 of *LNCS*, pages 729–738. Springer. ISBN 978-3-030-00928-1.
 - [28] Bob D. de Vos, Floris F. Berendsen, Max A. Viergever, Hessam Sokooti, Marius Staring, and Ivana Isgum. A deep learning framework for unsupervised affine and deformable image registration. *Med. Image Anal.*
 - [29] E. W. Dijkstra. A note on two problems in connexion with graphs. 1(1):269–271.
 - [30] Michal Drozdal, Eugene Vorontsov, Gabriel Chartrand, Samuel Kadoury, and Chris Pal. The importance of skip connections in biomedical image segmentation. In Gustavo Carneiro, Diana Mateus, Loïc Peter, Andrew Bradley, João Manuel R. S. Tavares, Vasileios Belagiannis, João Paulo Papa, Jacinto C. Nascimento, Marco Loog, Zhi Lu, Jaime S. Cardoso, and Julien Cornebise, editors, *Deep Learning and Data Labeling for Medical Applications*, volume 10008 of *LNCS*, pages 179–187. Springer. ISBN 978-3-319-46976-8. doi: 10.1007/978-3-319-46976-8_19.
 - [31] Aloys du Bois d’Aische, Mathieu De Craene, Xavier Geets, Vincent Gregoire, Benoit Macq, and Simon K. Warfield. Efficient multi-modal dense field non-rigid registration: alignment of histological and section images. *Med. Image Anal.*, 9(6):538–546. ISSN 1361-8415. doi: 10.1016/j.media.2005.04.003.
 - [32] Gunnar Farneback. Two-frame motion estimation based on polynomial expansion. In Josef Bigun and Tomas Gustavsson, editors, *Image Analysis*, volume 2749 of *LNCS*, pages 363–370. Springer. ISBN 978-3-540-40601-3. doi: 10.1007/3-540-45103-X_50.
 - [33] D. Fong and M. Saunders. LSMR: An iterative algorithm for sparse least-squares problems. *SIAM J. Sci. Comput.*, 33(5):2950–2971. doi: 10.1137/10079687X.
 - [34] Huazhu Fu, Yanwu Xu, Damon Wing Kee Wong, and Jiang Liu. Retinal vessel segmentation via deep learning network and fully-connected conditional random fields. In *2016 IEEE 13th International Symposium on Biomedical Imaging (ISBI)*, pages 698–701. doi: 10.1109/ISBI.2016.7493362. ISSN: 1945-8452.
 - [35] Alberto Garcia-Garcia, Sergio Orts-Escolano, Sergiu Oprea, Victor Villena-Martinez, and Jose Garcia-Rodriguez. A review on deep learning techniques applied to semantic segmentation. *arXiv:1704.06857 [cs]*. URL <http://arxiv.org/abs/1704.06857>.
 - [36] Marcel Gehring, Michal Tomaszewski, Dominick McIntyre, Jonathan Disselhorst, and Sarah Bohndiek. Co-registration of optoacoustic tomography and magnetic resonance imaging data from murine tumour models. *bioRxiv*, page 636035. doi: 10.1101/636035.
 - [37] Roman Grothausmann. Registration test data. GitHub, December 2019. URL https://github.com/romangrothausmann/elastix_scripts.
 - [38] Roman Grothausmann, Lars Knudsen, Matthias Ochs, and Christian Mühlfeld. Digital 3D reconstructions

- using histological serial sections of lung tissue including the alveolar capillary network. *Am. J. Physiol.-Lung C.*, 312(2):L243–L257. ISSN 1040-0605, 1522-1504. doi: 10.1152/ajplung.00326.2016.
- [39] Anna Gummesson, Ida Arvidsson, Mattias Ohlsson, Niels Christian Overgaard, Agnieszka Krzyzanowska, Anders Heyden, Anders Bjartell, and Kalle Aström. Automatic Gleason grading of H and E stained microscopic prostate images using deep convolutional neural networks. In *Medical Imaging 2017: Digital Pathology*, volume 10140, page 101400S. SPIE. doi: 10.1117/12.2253620.
- [40] Kan Guo, Dongqing Zou, and Xiaowu Chen. 3D mesh labeling via deep convolutional neural networks. *ACM T. Graphics.*, 35(1):1–12. ISSN 07300301. doi: 10.1145/2835487.
- [41] Eldad Haber and Jan Modersitzki. Intensity gradient based registration and fusion of multi-modal images. In Rasmus Larsen, Mads Nielsen, and Jon Sporring, editors, *Medical Image Computing and Computer-Assisted Intervention – MICCAI 2006*, LNCS, pages 726–733. Springer. ISBN 978-3-540-44728-3. doi: 10.1007/11866763_89.
- [42] Mattias P. Heinrich, Mark Jenkinson, Manav Bhushan, Tahreema Matin, Fergus V. Gleeson, Sir Michael Brady, and Julia A. Schnabel. MIND: Modality independent neighbourhood descriptor for multi-modal deformable registration. *Med. Image Anal.*, 16(7):1423–1435. ISSN 1361-8415. doi: 10.1016/j.media.2012.05.008.
- [43] Jerry L. Hintze and Ray D. Nelson. Violin plots: A box plot-density trace synergism. *Am. Stat.*, 52(2):181–184. doi: 10.1080/00031305.1998.10480559.
- [44] W. Huizinga, D.H.J. Poot, J.-M. Guyader, R. Klaassen, B.F. Coolen, M. van Kranenburg, R.J.M. van Geuns, A. Uitterdijk, M. Polfliet, J. Vandemeulebroucke, A. Leemans, W.J. Niessen, and S. Klein. PCA-based groupwise image registration for quantitative MRI. *Med. Image Anal.*, 29:65–78. ISSN 13618415. doi: 10.1016/j.media.2015.12.004.
- [45] Wyke Huizinga, Dirk H. J. Poot, Jean-Marie Guyader, Henk Smit, Matthijs van Kranenburg, Robert-Jan M. van Geuns, André Uitterdijk, Heleen M. M. van Beusekom, Bram F. Coolen, Alexander Leemans, Wiro J. Niessen, and Stefan Klein. Non-rigid groupwise image registration for motion compensation in quantitative MRI. In Sébastien Ourselin and Marc Modat, editors, *Biomedical Image Registration*, LNCS, pages 184–193. Springer. ISBN 978-3-319-08554-8. doi: 10.1007/978-3-319-08554-8_19.
- [46] Paul Jaccard. The distribution of the flora in the alpine zone. 11(2):37–50. ISSN 1469-8137. doi: 10.1111/j.1469-8137.1912.tb05611.x.
- [47] Chiyu Jiang, Dequan Wang, Jingwei Huang, Philip Marcus, and Matthias Nießner. Convolutional neural networks on non-uniform geometrical signals using Euclidean spectral transformation. In *International Conference on Learning Representations*, 2019.
- [48] Jun Jiang, Nicholas B. Larson, Naresh Prodduturi, Thomas J. Flotte, and Steven N. Hart. Robust hierarchical density estimation and regression for restained histological whole slide image co-registration. *PLOS ONE*, 14(7):e0220074. ISSN 1932-6203. doi: 10.1371/journal.pone.0220074.
- [49] Tao Ju. Robust repair of polygonal models. 23(3):888–895. ISSN 0730-0301. doi: 10.1145/1015706.1015815.
- [50] Adrian Kaehler and Gary Bradski. *Learning OpenCV*. O’Reilly, 2nd edition edition. ISBN 978-1-4493-3195-5.
- [51] Takehiro Kajihara, Takuya Funatomi, Haruyuki Makishima, Takahito Aoto, Hiroyuki Kubo, Shigehito Yamada, and Yasuhiro Mukaigawa. Non-rigid registration of serial section images by blending transforms for 3D reconstruction. *Pattern Recogn.*, 96:106956. ISSN 0031-3203. doi: 10.1016/j.patcog.2019.07.001.
- [52] Justin Ker, Lipo Wang, Jai Rao, and Tchoyoson Lim. Deep learning applications in medical image analysis. *IEEE Access*, 6:9375–9389. ISSN 2169-3536. doi: 10.1109/ACCESS.2017.2788044.
- [53] A. M. Khan, N. Rajpoot, D. Treanor, and D. Magee. A nonlinear mapping approach to stain normalization in digital histopathology images using image-specific color deconvolution. *IEEE T. Biomed. Eng.*, 61(6):1729–1738. ISSN 0018-9294. doi: 10.1109/TBME.2014.2303294.
- [54] Ron Kikinis, Steve D. Pieper, and Kirby G. Vossburgh. 3D Slicer: A platform for subject-specific image analysis, visualization, and clinical support. In Ferenc A. Jolesz, editor, *Intraoperative Imaging and Image-Guided Therapy*, pages 277–289. Springer. ISBN 978-1-4614-7657-3. doi: 10.1007/978-1-4614-7657-3_19.
- [55] S. Klein, M. Staring, K. Murphy, M. A. Viergever, and J. P. W. Pluim. elastix: A toolbox for intensity-based medical image registration. *IEEE T. Med. Imaging*, 29(1):196–205. ISSN 0278-0062. doi: 10.1109/TMI.2009.2035616.
- [56] Jens-Peer Kuska, Ulf-Dietrich Braumann, Nico Scherf, Markus Löffler, Jens Einenkel, Michael Hockel, Lars-Christian Horn, Nicolas Wentzensen, and Magnus von Knebel Doeberitz. Image registration of differently stained histological sections. In *2006 International Conference on Image Processing*, pages 333–336. doi: 10.1109/ICIP.2006.313161.
- [57] Matthew Lai. Deep learning for medical image segmentation. *arXiv:1505.02000 [cs]*. URL <http://arxiv.org/abs/1505.02000>.
- [58] Gudrun Lang. *Histotechnik: Praxislehrbuch für die Biomedizinische Analytik*. Springer Science & Business Media. ISBN 978-3-211-33141-5. Google-Books-ID: FulU0tG7kaQC.
- [59] Daewon Lee, Matthias Hofmann, Florian Steinke, Yasemin Altun, Nathan D Cahill, and Bernhard Scholkopf. Learning similarity measure for multi-modal 3D image registration. In *IEEE Conference on Computer Vision and Pattern Recognition*, pages 186–193. IEEE, 2009.
- [60] Carlos Leiva-Salinas, Thomas J. Eluvathingal Muttikkal, Lucia Flors, Josep Puig, Max Wintermark, James T. Patrie, Patrice K. Rehm, Jason P. Sheehan, and David Schiff. FDG PET/MRI coregistration helps predict response to gamma knife radiosurgery in patients with brain metastases. *Am. J. Roentgenol.*, 212(2):425–430. ISSN 0361-803X. doi: 10.2214/AJR.18.20006.
- [61] Zhengxiao Li and James Bethel. Image coregistration in SAR interferometry. *Int. Arch. Photogramm. Remote Sens. Spat. Inf. Sci.*, 37:433–438.
- [62] Yiyi Liao, Simon Donné, and Andreas Geiger. Deep marching cubes: Learning explicit surface representations. In *Proceedings of the IEEE Conference on Computer Vision and Pattern Recognition*, pages 2916–2925.
- [63] Giuseppe Lippolis, Anders Edsjö, Leszek Helczynski, Anders Bjartell, and Niels Chr Overgaard. Automatic registration of multi-modal microscopy images for inte-

- grative analysis of prostate tissue sections. *BMC Cancer*, 13(1). ISSN 1471-2407. doi: 10.1186/1471-2407-13-408.
- [64] Geert Litjens, Thijs Kooi, Babak Ehteshami Bejnordi, Arnaud Arindra Adiyoso Setio, Francesco Ciompi, Mohsen Ghafoorian, Jeroen A. W. M. van der Laak, Bram van Ginneken, and Clara I. Sánchez. A survey on deep learning in medical image analysis. *Med. Image Anal.*, 42:60–88, . ISSN 1361-8415. doi: 10.1016/j.media.2017.07.005.
- [65] Geert Litjens, Clara I. Sánchez, Nadya Timofeeva, Meyke Hermesen, Iris Nagtegaal, Iringo Kovacs, Christina Hulsbergen-van de Kaa, Peter Bult, Bram van Ginneken, and Jeroen van der Laak. Deep learning as a tool for increased accuracy and efficiency of histopathological diagnosis. *Sci. Rep.*, 6:26286, . ISSN 2045-2322. doi: 10.1038/srep26286.
- [66] Oleg Lobachev. On three-dimensional reconstruction. URL <https://epub.uni-bayreuth.de/3774/>.
- [67] Oleg Lobachev, Birte S. Steiniger, and Michael Guthe. Compensating anisotropy in histological serial sections with optical flow-based interpolation. In *Proceedings of the 33rd Spring Conference on Computer Graphics, SCCG '17*, pages 14:1–14:11, New York, NY, USA, 2017. ACM. ISBN 978-1-4503-5107-2. doi: 10.1145/3154353.3154366.
- [68] Oleg Lobachev, Christine Ulrich, Birte S. Steiniger, Verena Wilhelmi, Vitus Stachniss, and Michael Guthe. Feature-based multi-resolution registration of immunostained serial sections. *Med. Image Anal.*, 35:288–302, January 2017. ISSN 1361-8415. doi: 10.1016/j.media.2016.07.010.
- [69] William E. Lorensen and Harvey E. Cline. Marching cubes: A high resolution 3D surface construction algorithm. *SIGGRAPH Comput. Graph.*, 21(4):163–169. ISSN 0097-8930. doi: 10.1145/37402.37422.
- [70] Peter Lorenzen, Marcel Prastawa, Brad Davis, Guido Gerig, Elizabeth Bullitt, and Sarang Joshi. Multi-modal image set registration and atlas formation. *Med. Image Anal.*, 10(3):440–451. ISSN 1361-8415. doi: 10.1016/j.media.2005.03.002.
- [71] Boyuan Ma, Xiaojuan Ban, Haiyou Huang, Yulian Chen, Wanbo Liu, and Yonghong Zhi. Deep learning-based image segmentation for al-la alloy microscopic images. *Symmetry*, 10(4):107, . doi: 10.3390/sym10040107.
- [72] Kai Ma, Jiangping Wang, Vivek Singh, Birgi Tamer-soy, Yao-Jen Chang, Andreas Wimmer, and Terrence Chen. Multimodal image registration with deep context reinforcement learning. In Maxime Descoteaux, Lena Maier-Hein, Alfred Franz, Pierre Jannin, D. Louis Collins, and Simon Duchesne, editors, *Medical Image Computing and Computer Assisted Intervention — MICCAI 2017*, LNCS, pages 240–248. Springer, . ISBN 978-3-319-66182-7. doi: 10.1007/978-3-319-66182-7_28.
- [73] Dwarikanath Mahapatra, Bhavna Antony, Suman Sedai, and Rahil Garnavi. Deformable medical image registration using generative adversarial networks. In *2018 IEEE 15th International Symposium on Biomedical Imaging (ISBI 2018)*, pages 1449–1453. doi: 10.1109/ISBI.2018.8363845.
- [74] Jan Michálek, Karel Štěpka, Michal Kozubek, Jarmila Navrátilová, Barbora Pavlatovská, Markéta Machálková, Jan Preisler, and Adam Pruška. Quantitative assessment of anti-cancer drug efficacy from coregistered mass spectrometry and fluorescence microscopy images of multicellular tumor spheroids. *Microsc. Microanal.* ISSN 1431-9276, 1435-8115. doi: 10.1017/S1431927619014983.
- [75] Fausto Milletari, Nassir Navab, and Seyed-Ahmad Ahmadi. V-Net: Fully convolutional neural networks for volumetric medical image segmentation. In *2016 Fourth International Conference on 3D Vision (3DV)*, pages 565–571. doi: 10.1109/3DV.2016.79.
- [76] Kishore Mosaliganti, Tony Pan, Richard Sharp, Randall Ridgway, Srivathsan Iyengar, Alexandra Gulacy, Pamela Wenzel, Alain de Bruin, Raghu Machiraju, Kun Huang, Gustavo Leone, and Joel Saltz. Registration and 3D visualization of large microscopy images. page 61442V. doi: 10.1117/12.653505.
- [77] Dan Mueller, Dirk Vossen, and Bas Hulsken. Real-time deformable registration of multi-modal whole slides for digital pathology. *Comput. Med. Imag. Grap.*, 35(7): 542–556. ISSN 0895-6111. doi: 10.1016/j.compmedimag.2011.06.006.
- [78] Devrim Onder, Selen Zengin, and Sulen Sarioglu. A review on color normalization and color deconvolution methods in histopathology. *Appl. Immunohistochem. Mol. Morphol.*, 22(10):713–719. ISSN 1541-2016. doi: 10.1097/PAI.0000000000000003.
- [79] Hector Ortega-Arranz, Yuri Torres, Arturo Gonzalez-Escribano, and Diego R. Llanos. Comprehensive evaluation of a new GPU-based approach to the shortest path problem. *Int. J. Parallel Prog.*, 43(5):918–938. ISSN 0885-7458, 1573-7640. doi: 10.1007/s10766-015-0351-z.
- [80] S. Ourselin, A. Roche, G. Subsol, X. Pennec, and N. Ayache. Reconstructing a 3D structure from serial histological sections. *Image Vis. Comput.*, 19(1):25–31, . doi: 10.1016/S0262-8856(00)00052-4.
- [81] Sébastien Ourselin, Radu Stefanescu, and Xavier Pennec. Robust registration of multi-modal images: Towards real-time clinical applications. In Takeyoshi Dohi and Ron Kikinis, editors, *Medical Image Computing and Computer-Assisted Intervention — MICCAI 2002*, LNCS, pages 140–147. Springer, . ISBN 978-3-540-45787-9. doi: 10.1007/3-540-45787-9_18.
- [82] Hyunjin Park, Morand R. Piert, Asra Khan, Rajal Shah, Hero Hussain, Javed Siddiqui, Thomas L. Chenevert, and Charles R. Meyer. Registration methodology for histological sections and in vivo imaging of human prostate. *Acad. Radiol.*, 15(8):1027–1039. ISSN 1076-6332. doi: 10.1016/j.acra.2008.01.022.
- [83] Nathan Heath Patterson, Ethan Yang, Elizabeth-Ann Kranjec, and Pierre Chaurand. Co-registration and analysis of multiple imaging mass spectrometry datasets targeting different analytes. *Bioinformatics*, 35(7):1261–1262. ISSN 1367-4803. doi: 10.1093/bioinformatics/bty780.
- [84] Jonas Pichat, Juan Eugenio Iglesias, Tarek Yousry, Sébastien Ourselin, and Marc Modat. A survey of methods for 3D histology reconstruction. *Med. Image Anal.*, 46:73–105. ISSN 13618415. doi: 10.1016/j.media.2018.02.004.
- [85] S. Pieper, M. Halle, and R. Kikinis. 3D Slicer. In *IEEE International Symposium on Biomedical Imaging: Nano to Macro*, volume 1, pages 632–635. doi: 10.1109/ISBI.2004.1398617.
- [86] Mathias Polfiet, Stefan Klein, Wyke Huizinga, Margarethus M. Paulides, Wiro J. Niessen, and Jef Vandemeulebroucke. Intrasubject multimodal group-wise registration with the conditional template entropy.

- Med. Image Anal.*, 46:15–25. ISSN 13618415. doi: 10.1016/j.media.2018.02.003.
- [87] Adhish Prasoon, Kersten Petersen, Christian Igel, François Lauze, Erik Dam, and Mads Nielsen. Deep feature learning for knee cartilage segmentation using a triplanar convolutional neural network. In Kensaku Mori, Ichiro Sakuma, Yoshinobu Sato, Christian Barillot, and Nassir Navab, editors, *Medical Image Computing and Computer-Assisted Intervention – MICCAI 2013*, volume 8150 of *LNCS*, pages 246–253. Springer. ISBN 978-3-642-40763-5. doi: 10.1007/978-3-642-40763-5_31.
- [88] Charles R. Qi, Hao Su, Matthias Niessner, Angela Dai, Mengyuan Yan, and Leonidas J. Guibas. Volumetric and multi-view CNNs for object classification on 3D data. In *Proceedings of the IEEE Conference on Computer Vision and Pattern Recognition*, pages 5648–5656.
- [89] E. Reinhard, M. Adhikhmin, B. Gooch, and P. Shirley. Color transfer between images. *IEEE Comput. Graph.*, 21(5):34–41. ISSN 0272-1716. doi: 10.1109/38.946629.
- [90] N. Salamon, J. Kung, S. J. Shaw, J. Koo, S. Koh, J. Y. Wu, J. T. Lerner, R. Sankar, W. D. Shields, J. Engel, I. Fried, H. Miyata, W. H. Yong, H. V. Vinters, and G. W. Mathern. FDG-PET/MRI coregistration improves detection of cortical dysplasia in patients with epilepsy. *Neurology*, 71(20):1594–1601. ISSN 0028-3878, 1526-632X. doi: 10.1212/01.wnl.0000334752.41807.2f.
- [91] Kadharbatchesa S. Saleem and Nikos K. Logothetis. *A combined MRI and histology atlas of the rhesus monkey brain in stereotaxic coordinates*. Academic Press. ISBN 978-0-12-385087-4.
- [92] Oliver Schmitt, Jan Modersitzki, Stefan Heldmann, Stefan Wirtz, and Bernd Fischer. Image registration of sectioned brains. *Int. J. Comput. Vision.*, 73(1):5–39. ISSN 1573-1405. doi: 10.1007/s11263-006-9780-x.
- [93] M. Tarek Shaban, Christoph Baur, Nassir Navab, and Shadi Albarqouni. Staingan: Stain style transfer for digital histological images. In *2019 IEEE 16th International Symposium on Biomedical Imaging (ISBI 2019)*, pages 953–956. doi: 10.1109/ISBI.2019.8759152.
- [94] Martin Simonovsky, Benjamín Gutiérrez-Becker, Diana Mateus, Nassir Navab, and Nikos Komodakis. A deep metric for multimodal registration. In Sebastien Ourselin, Leo Joskowicz, Mert R. Sabuncu, Gozde Unal, and William Wells, editors, *Medical Image Computing and Computer-Assisted Intervention - MICCAI 2016*, volume 9902 of *LNCS*, pages 10–18. Springer. ISBN 978-3-319-46726-9. doi: 10.1007/978-3-319-46726-9_2.
- [95] Vincent Sitzmann, Justus Thies, Felix Heide, Matthias Niessner, Gordon Wetzstein, and Michael Zollhofer. DeepVoxels: Learning persistent 3D feature embeddings. In *The IEEE Conference on Computer Vision and Pattern Recognition (CVPR)*, pages 2437–2446, June 2019.
- [96] Y. Song, D. Treanor, A. J. Bulpitt, N. Wijayathunga, N. Roberts, R. Wilcox, and D. R. Magee. Unsupervised content classification based nonrigid registration of differently stained histology images. *IEEE T. Bio-Med. Eng.*, 61(1):96–108, . ISSN 0018-9294. doi: 10.1109/TBME.2013.2277777.
- [97] Y Song, D Treanor, AJ Bulpitt, and DR Magee. 3D reconstruction of multiple stained histology images. *J. Pathol. Inform.*, 4(2):7, .
- [98] Lilian Steffen, Clemens Ruppert, Heinz-Gerd Hoymann, Manuela Funke, Simone Ebner, Christina Kloth, Christian Mühlfeld, Matthias Ochs, Lars Knudsen, and Elena Lopez-Rodriguez. Surfactant replacement therapy reduces acute lung injury and collapse induration-related lung remodeling in the bleomycin model. *Am. J. Physiol.-Lung C.*, 313(2):L313–L327. ISSN 1040-0605. doi: 10.1152/ajplung.00033.2017.
- [99] B S Steiniger, V Wilhelmi, M Berthold, M Guthe, and O Lobachev. Locating human splenic capillary sheaths in virtual reality. *Sci. Rep.*, 8(1):10, 2018. ISSN 2045-2322. doi: 10.1038/s41598-018-34105-3.
- [100] B. S. Steiniger, H. Pfeffer, M. Guthe, and O. Lobachev. The human splenic red pulp vasculature from terminal arteries to venules in virtual reality. details of sheathed capillaries and the open capillary network. unpublished, 2019.
- [101] Birte S Steiniger, Christine Ulrich, Moritz Berthold, Michael Guthe, and Oleg Lobachev. Capillary networks and follicular marginal zones in human spleens. three-dimensional models based on immunostained serial sections. *PLOS ONE*, 13:21, 02 2018. doi: 10.1371/journal.pone.0191019.
- [102] Lisa Tang, Alfred Hero, and Ghassan Hamarneh. Locally-adaptive similarity metric for deformable medical image registration. In *2012 9th IEEE International Symposium on Biomedical Imaging (ISBI)*, pages 728–731. doi: 10.1109/ISBI.2012.6235651. ISSN: 1945-8452, 1945-7928, 1945-7928.
- [103] Gabriel Taubin. A signal processing approach to fair surface design. In *Proceedings of the 22nd Annual Conference on Computer Graphics and Interactive Techniques, SIGGRAPH '95*, pages 351–358. ACM. ISBN 978-0-89791-701-8. doi: 10.1145/218380.218473.
- [104] Neslisah Torosdagli, Mary McIntosh, Denise K. Liberton, Payal Verma, Murat Sincan, Wade W. Han, Janice S. Lee, and Ulas Bagci. Relational reasoning network (RRN) for anatomical landmarking. *arXiv:1904.04354 [cs, stat]*. URL <http://arxiv.org/abs/1904.04354>.
- [105] Nicholas Trahearn, David Epstein, Ian Cree, David Snead, and Nasir Rajpoot. Hyper-stain inspector: A framework for robust registration and localised co-expression analysis of multiple whole-slide images of serial histology sections. *Sci. Rep.*, 7(1). ISSN 2045-2322. doi: 10.1038/s41598-017-05511-w.
- [106] Ch Ulrich, O. Lobachev, B. S. Steiniger, and M. Guthe. Imaging the vascular network of the human spleen from immunostained serial sections. In *Visual Computing for Biology and Medicine*, VCBM '14. Eurographics.
- [107] Christian Wachinger and Nassir Navab. Entropy and Laplacian images: Structural representations for multimodal registration. *Med. Image Anal.*, 16(1):1–17. ISSN 1361-8415. doi: 10.1016/j.media.2011.03.001.
- [108] Guotai Wang, Wenqi Li, Maria A. Zuluaga, Rosalind Pratt, Premal A. Patel, Michael Aertsen, Tom Doel, Anna L. David, Jan Deprest, Sébastien Ourselin, and Tom Vercauteren. Interactive medical image segmentation using deep learning with image-specific fine tuning. *IEEE T. Med. Imaging*, 37(7):1562–1573, . ISSN 0278-0062, 1558-254X. doi: 10.1109/TMI.2018.2791721.
- [109] Zhou Wang, A.C. Bovik, H.R. Sheikh, and E.P. Simoncelli. Image quality assessment: from error visibility to structural similarity. *IEEE T. Image Process.*, 13(4):600–612, . ISSN 1057-7149. doi: 10.1109/TIP.2003.819861.
- [110] Nicolas Wentzensen, Ulf-Dietrich Braumann, Jens Eienkel, Lars-Christian Horn, Magnus von Knebel Doeberitz, Markus Löffler, and Jens-Peer Kuska. Combined

- serial section-based 3D reconstruction of cervical carcinoma invasion using H&E/p16INK4a/CD3 alternate staining. *Cytom. Part A*, 71A(5):327–333. ISSN 1552-4930. doi: 10.1002/cyto.a.20385.
- [111] Guorong Wu, Hongjun Jia, Qian Wang, and Dinggang Shen. SharpMean: Groupwise registration guided by sharp mean image and tree-based registration. *NeuroImage*, 56(4):1968–1981. ISSN 1053-8119. doi: 10.1016/j.neuroimage.2011.03.050.
- [112] Yan Xu, Tao Mo, Qiwei Feng, Peilin Zhong, Maode Lai, and Eric I-Chao Chang. Deep learning of feature representation with multiple instance learning for medical image analysis. In *2014 IEEE International Conference on Acoustics, Speech and Signal Processing (ICASSP)*, pages 1626–1630. IEEE. ISBN 978-1-4799-2893-4. doi: 10.1109/ICASSP.2014.6853873.
- [113] Farhad Ghazvinian Zanjani, Svitlana Zinger, Babak Ehteshami Bejnordi, Jeroen A W M van der Laak, and Peter H. N. de With. Stain normalization of histopathology images using generative adversarial networks. In *2018 IEEE 15th International Symposium on Biomedical Imaging (ISBI 2018)*, pages 573–577. IEEE. ISBN 978-1-5386-3636-7. doi: 10.1109/ISBI.2018.8363641.
- [114] Andy Zeng, Shuran Song, Matthias Niessner, Matthew Fisher, Jianxiong Xiao, and Thomas Funkhouser. 3DMatch: Learning local geometric descriptors from RGB-D reconstructions. In *Proceedings of the IEEE Conference on Computer Vision and Pattern Recognition*, pages 1802–1811.
- [115] He Zhang, Vishwanath Sindagi, and Vishal M. Patel. Image de-raining using a conditional generative adversarial network. *IEEE T. Circ. Syst. Vid.* doi: 10.1109/TCSVT.2019.2920407.
- [116] S. Kevin Zhou, Hayit Greenspan, and Dinggang Shen. *Deep Learning for Medical Image Analysis*. Academic Press. ISBN 978-0-12-810409-5. Google-Books-ID: WVqfDAAAQBAJ.